Devonian F-rich peraluminous A-type magmatism in the proto-Andean foreland (Sierras Pampeanas, Argentina): geochemical constraints and petrogenesis from the western-central region of the Achala batholith

Juan A. Dahlquist, Pablo H. Alasino & Carina Bello

Mineralogy and Petrology

ISSN 0930-0708
Volume 108
Number 3

Miner Petrol (2014) 108:391-417
DOI 10.1007/s00710-013-0308-0

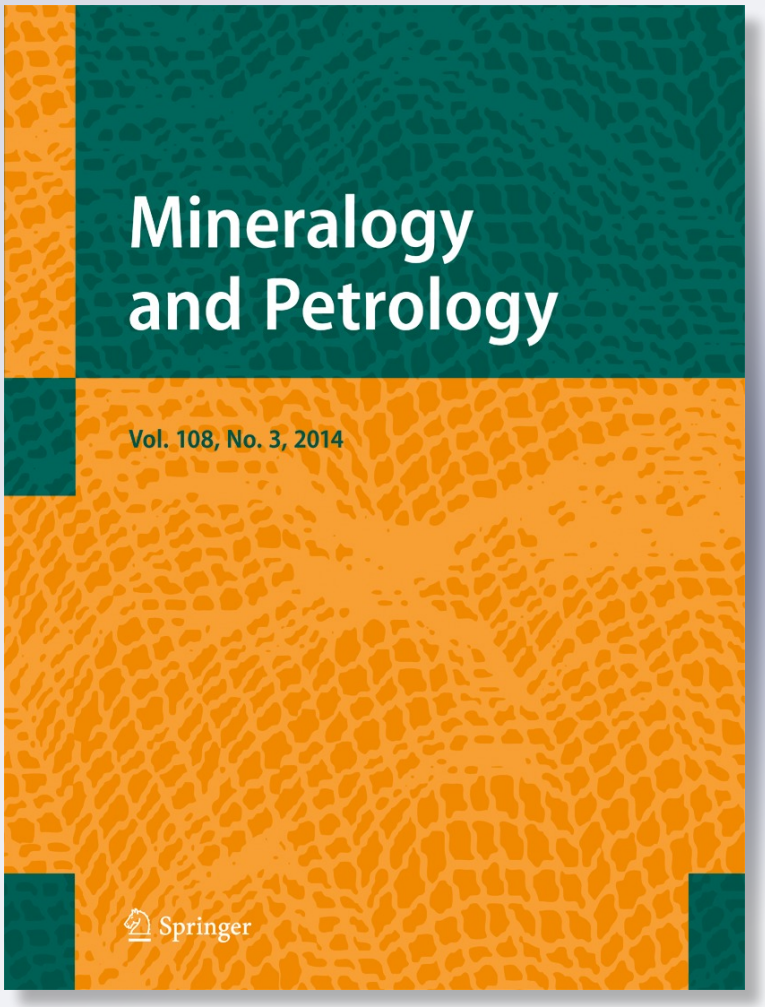

Springer

Miner Petrol (2014) 108:391–417
DOI 10.1007/s00710-013-0308-0

ORIGINAL PAPER

Devonian F-rich peraluminous A-type magmatism in the proto-Andean foreland (Sierras Pampeanas, Argentina): geochemical constraints and petrogenesis from the western-central region of the Achala batholith

Juan A. Dahlquist · Pablo H. Alasino · Carina Bello

Received: 7 May 2013 / Accepted: 21 August 2013 / Published online: 15 September 2013

Abstract A new LA-ICP-MS crystallization age of 370± 8 Ma is presented for monzogranite from the Achala batholith, the largest Devonian igneous body in the Sierras Pampeanas, confirming previous U-Pb zircon ages and indicating emplacement within a relatively short episode. Granitic rocks from the central area of the batholith display restricted high SiO_2 contents (69.8–74.5 wt.%). Major element plots show ferroan and alkaline-calcic to calc-alkaline compositions with an A-type signature. High concentrations of the high field-strength elements such as Y, Nb, Ga, Ta, U, Th, and flat REE patterns with significant negative Eu anomalies, are also typical of A-type granites. The aluminium saturation index (1.10–1.37) indicates aluminous parent magmas which are further characterised by high FeO/MgO ratios (2.6–3.3) and F contents of igneous biotites (0.9–1.5 wt%), as well as relatively high Al^{IV} (2.39–2.58 a.p.f.u.) in biotites and the occurrence of primary muscovite. Petrogenetic modelling supports a source enriched in plagioclase and progressive fractional crystallization of feldspar. The central area of the batholith displays small-scale bodies composed predominantly of biotite (80 %), muscovite (10 %) and apatite (10 %), yielding rock compositions with 2.3–5.4 wt. % P_2O_5, and 6–7 wt.% F, together with anomalous contents of U (88–1,866 ppm), Zr (1081–2,581 ppm), Nb (257–1,395 ppm) and ΣREE (1,443–4,492 ppm). Previous studies rule out an origin of these bodies as metasedimentary xenoliths and they have been interpreted as cumulates from the granitic magma. An alternative flow segregation process is discussed here.

Editorial handling: G. Hoinkes

J. A. Dahlquist (✉)
CICTERRA-CONICET-UNC, Av. Vélez Sarsfield 1611, CICTERRA building, X5016CGA Córdoba, Argentina
e-mail: jdahlquist@efn.uncor.edu

P. H. Alasino
INGeReN-CENIIT-UNLaR, Av. Gob. Vernet y Apóstol Felipe, 5300 La Rioja, Argentina

P. H. Alasino
CRILAR-CONICET, Entre Ríos y Mendoza, 5301 Anillaco, La Rioja, Argentina

C. Bello
Regional Centro, Comisión Nacional de Energía Atómica, Espinel 902, 5000 Córdoba, Argentina

Introduction

A variety of systematic studies during the past 10 years have improved our understanding of the petrogenesis and timing of the Pampean and Famatinian granitoids, but the late Palaeozoic granites (i.e., Devonian and Carboniferous) emplaced in the Eastern Sierras Pampeanas after the metamorphic peak of the Famatinian Orogeny have received relatively little attention until recently.

Our understanding of the petrogenesis of the Carboniferous granite of Sierras Pampeanas has been improved in the last years (e.g., Dahlquist et al. 2006, 2010, 2013; Alasino et al. 2012 and references therein), but the petrogenesis of the Middle-Late Devonian magmatism is still not well constrained (e.g., Siegesmund et al. 2004; López de Luchi et al. 2007).

The largest batholith of Devonian age, the Achala batholith (Sierras de Córdoba), is considered a typical result of this magmatism and consistently was termed the *Achalian* orogen by Sims et al. (1998). Studies of the Middle-Late Devonian magmatism have been carried out on granites in the Sierra de San Luis (e.g., Siegesmund et al. 2004; López de Luchi et al. 2007). However, there is no consensus about the petrogenesis of this magmatism, which has been considered as arc-related with some syncollisional and even a

within-plate setting for the more evolved granitoids (López de Luchi et al. 2007).

Although the Achala batholith is one of the largest intrusive granitic bodies in the Sierras Pampeanas, petrological, geochemical, isotopical, and geochronological data have been poorly and discontinuously reported. A seminal paper by Rapela (1982) based on petrological and geochemical data using major element and some trace elements concluded that the Achala batholith is a postkinematic peraluminous calcalkaline body but with 'alkalic' characteristics probably related to the pre-rift uplifting of the area after the Lower Paleozoic orogenic events.

Subsequently Lira and Kirschbaum (1990) reported petrological and geochemical studies using major and some trace elements (excluding REE, U, Nb, etc.) in the central area of the batholith. These authors concluded that the Achala granitoids have geochemical affinities both S-type and within-plate granites.

Dorais et al. (1997) studied the central Achala batholith area where the granites bear unusual biotite-apatite bodies (called 'layered enclaves' by Dorais et al. 1997, see discussion in Sections Geology of the Achala batholith and Biotite-apatite bodies) characterized by 89–93 % biotite with high FeO/MgO ratios (mean 3.1), 7–11 % apatite and high F contents (mean 3.5 %); they have abundant zircon and monazite together with scarce oxides as accessory minerals. This modal mineralogy produces unusual bulk-rock compositions, showing remarkably high abundances of P_2O_5, F and some trace elements (P_2O_5=1–8 wt.%, F=0.7–1.7 wt.%, U=26–235 ppm, Zr=835–2,800 ppm, and ΣREE=998–5,275 ppm). Dorais et al. (1997) reported whole-rock and mineral chemistry for these bodies, but not the composition of the host granites.

Recently, Rapela et al. (2008a) reported conclusions based on whole-rock chemistry, Nd isotopes, and geochronological information in a short paper, but the data remain unpublished; they showed that the granitic rocks are peraluminous throughout the range of silica content, from 60 to 76 %, and show geochemical signatures typical of peraluminous A-type granites.

The present work is a contribution to the understanding the Devonian magmatism in the proto-Andean foreland, Sierras Pampeanas, Argentina. We present major and trace element data for 25 whole-rock samples, mineral compositions, and Sm-Nd isotope data for granitic rocks and unusual biotite-apatite bodies collected from the central region of the Achala batholith. In addition a new LA-ICP-MS U-Pb zircon crystallization age is reported here, confirming previous ages for the emplacement of the granitic rocks. Based on our new petrological, mineral chemistry, bulk major and trace element, Nd isotopes compositions and geochronological data, together with previous Hf and Nd isotopes compositions and geochronological data recently reported by Dahlquist et al. (2013), we assess the petrogenesis of the Achala batholith and discuss the origin of unusual biotite-apatite bodies. These biotite-apatite bodies have additional interest because of their economic potential, containing remarkably high concentrations of uranium and REE.

Geological setting

Using geochronological data and association with major orogenic episodes, four main granitoid groups have been recognized in the Eastern Sierras Pampeanas (including main references only): *Pampean magmatism*, 555−515 Ma; Rapela et al. (1998, 2007), Sims et al. (1998), Schwartz et al. (2008); *Famatinian magmatism*, 484−463 Ma; Pankhurst et al. (1998, 2000), Rapela et al. (2008b), Dahlquist et al. (2008, 2012), Ducea et al. (2010), and Casquet et al. (2011); *Achalian magmatism*, 393−366; Dorais et al. (1997), Sims et al. (1998), Stuart-Smith et al. (1999), Siegesmund et al. (2004), Rapela et al. (2008a); and *Early Carboniferous magmatism*, 357−322; Dahlquist et al. (2006), Grosse et al. (2009), Dahlquist et al. (2010), Alasino et al. (2012).

The ca. 2,500 km^2 Achala batholith in the Sierras de Córdoba (Fig. 1) was emplaced during the Late Devonian: 368±25 Ma U–Pb zircon (Dorais et al. 1997), 379±4 and 369±3 Ma U–Pb SHRIMP zircon (Rapela et al. 2008a), and 366±6, 369±5, and 372±6 Ma U–Pb LA-ICP-Ms zircon (Dahlquist et al. 2013). It is the largest of a series of intrusive granitic bodies in the Sierras Pampeanas that are conspicuously discordant to structures and rocks formed during the Cambrian (Pampean) and Ordovician (Famatinian) metamorphic events (Martino et al. 1995; Rapela et al. 2008b). Achala batholith has an A-type signature (Rapela et al. 2008a) and contact aureoles indicate shallow emplacement, usually at less than 2 kb (e.g., Patiño and Patiño Douce 1987; Baldo 1992; and Pinotti et al. 2002 data from the Cerro Aspero batholith of Late Devonian age, Fig. 1).

Sims et al. (1998), Stuart-Smith et al. (1999), and Siegesmund et al. (2004) considered the voluminous Devonian intrusive rocks in the Sierras de Córdoba and the eastern area of the Sierra de San Luis to have been emplaced during compression associated with Late Devonian low-grade shear zones, together defining the Achalian orogeny (Middle-to-Late Devonian). According to this interpretation the Devonian granites, such as the Achala (Sims et al. 1998) and Cerro Áspero batholiths in Sierra de Córdoba (e.g., Pinotti et al. 2002, 2006), and the Las Chacras-Potrerillos (Siegesmund et al., 2004) and Renca (Stuart-Smith et al. 1999) batholiths in Sierra de San Luis (Fig. 1), are not post-orogenic intrusions of the Famatinian Orogeny as proposed by Pankhurst and Rapela (1998), but belong to a distinct tectonomagmatic event.

The tectonic setting of the Late Devonian compressional event is controversial and has been related to: (i) collision of the hypothetical Chilenia terrane with the proto-Pacific margin (Willner et al. 2011 and references therein), (ii) final collision between the Famatinian magmatic arc and the Pampean

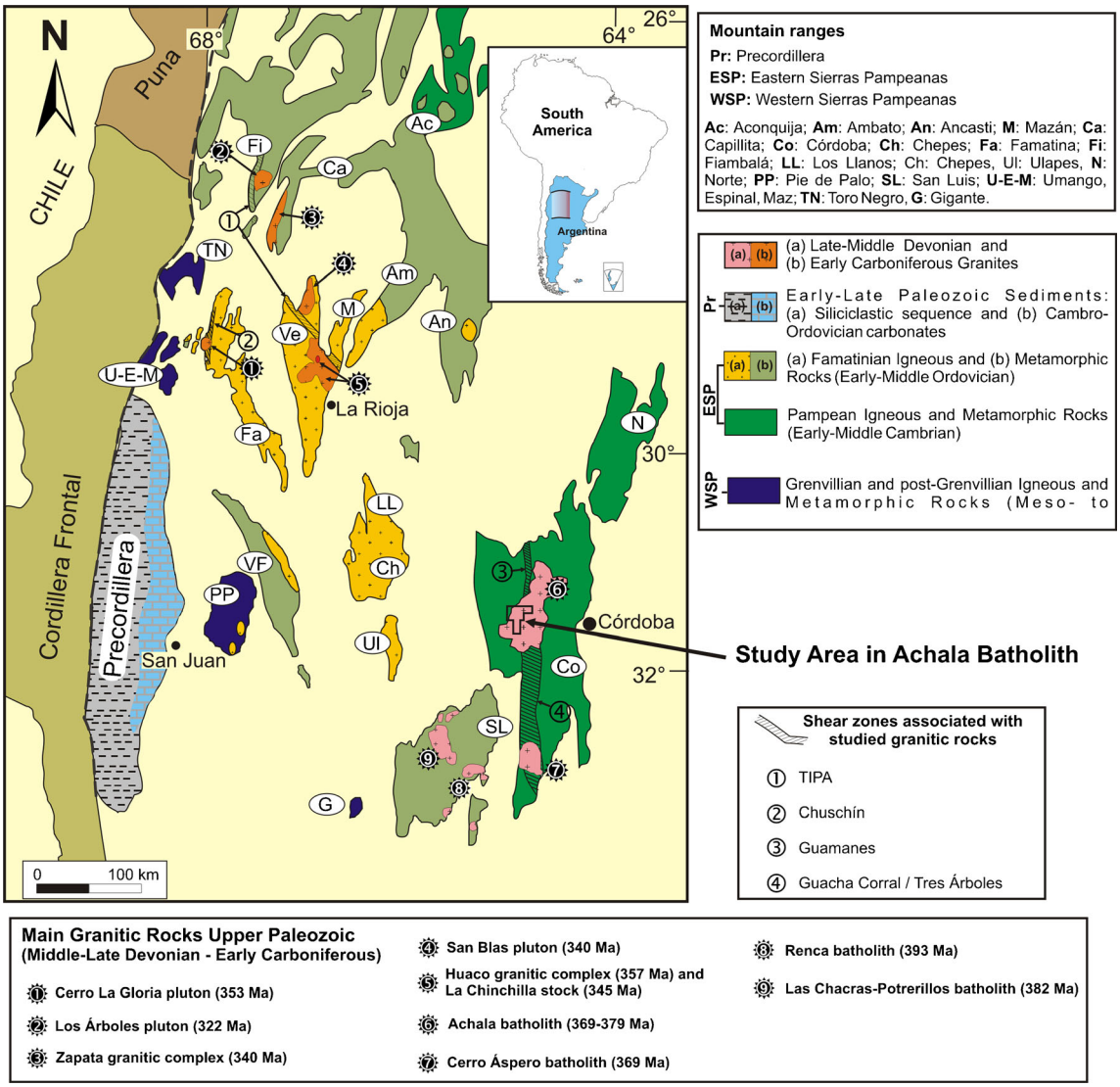

Fig. 1 Simplified geological map of west-central Argentina (Sierras Pampeanas), central Chile, and the location of the studied region in the Achala batholith. Main Devonian batholiths in Sierras Pampeanas are located in the map. Ages from Dahlquist et al. (2012, 2013), Grosse et al. (2009), Stuart-Smith et al. (1999), Siegesmund et al. (2004), and Rapela et al. (2008b). Post-Paleozoic cover in yellow. **Inset:** *rectangle* shows the location of Sierras Pampeanas in a regional sketch map of Argentina

hinterland (Höckenreiner et al. 2003) and, recently, (iii) push–pull tectonic switching episodes during Devonian and Carboniferous time, resulting from flat-slab/roll-back subduction along the Pacific margin (Alasino et al. 2012). The A-type geochemical signature of the Achala batholith (Rapela et al. 2008a) strongly suggests intracratonic magmatism in a dominantly extensional regime with Early–Middle Devonian? lithospheric thinning. This hypothesis is consistent with a Devonian metallogenetic epoch (~ 390 Ma) developed in an extensional setting temporally and spatially related to the Achala magmatism (Franchini et al. 2005). This extensional regime was followed by Late Devonian compressional event (Sims et al. 1998) and Early Carboniferous lithospheric stretching (Dahlquist et al. 2010). Thus, tectonic switching episodes of roll-back and flat-slab subduction (see Collins 2002) could have led to alternating compression and extension setting in the proto-Andean foreland (e.g., Alasino et al. 2012; Dahlquist et al. 2013).

Geology of the Achala batholith

The Achala batholith of the Sierras de Córdoba is largely dominated by monzogranitic units. Emplaced at 7–10 km depth (Baldo 1992), the granitic units define a NNE roughly elliptic body, 105 km long (Figs. 1 and 2).

The granites sharply cut the regional foliation (Martino et al. 1995) of Cambrian gneisses and migmatites related to the 555 −515 Ma Pampean orogeny (Rapela et al. 1998, 2007; Sims et al. 1998; Schwartz et al. 2008). They also cut N–S

Ordovician mylonite shear zones associated with the Famatinian orogeny (470–450 Ma, Martino 2003; Simpson et al. 2003), although these exhibit a low-temperature reactivation (Bt-Ms-Chl), probably synchronous with the development of magmatic shear fabric observed in the Achala batholith (Martino 2003; Zarco 2006).

Five main rock types (or facies, designated as A, B, C, D, and E) were recognized in the Achala batholith by Lira and Kirchbaum (1990) and Dorais et al. (1997) on the basis of granitic texture and modal composition (Fig. 2). Based on these previous studies and Zarco (2006), six main granitic facies have been recently recognized by Rapela et al. (2008a) (Fig. 2):

Facies 1. Medium-grained ± porphyritic monzogranite, located in the central sector of the batholith, is the most abundant, and consists of 1–3 cm Kfs phenocrysts set in a 2–3 mm equigranular matrix of Qtz-Kfs-Pl-Bt-Ms-Ap-Zrn-Op (mineral abbreviations from Kretz 1983). Facies 2. Coarse-grained porphyritic monzogranite located at the margins of the body, the second most abundant facies, probably formed earlier in the history of the batholith. These coarse granites show 3–5 cm Kfs megacrysts in a 3–5 mm equigranular matrix of Qtz-Kfs-Pl-Bt-Ms-Ap-Zrn-Op.

The remaining facies represent about 10–12 % of the batholith:

Facies 3. Medium-grained equigranular monzogranite, often leucocratic, includes muscovite and muscovite + biotite varieties, located at the northern and southern tips of the body (i.e., Cerro Champaquí, Mesa del Palmar and La Cumbrecita areas, Fig. 2).

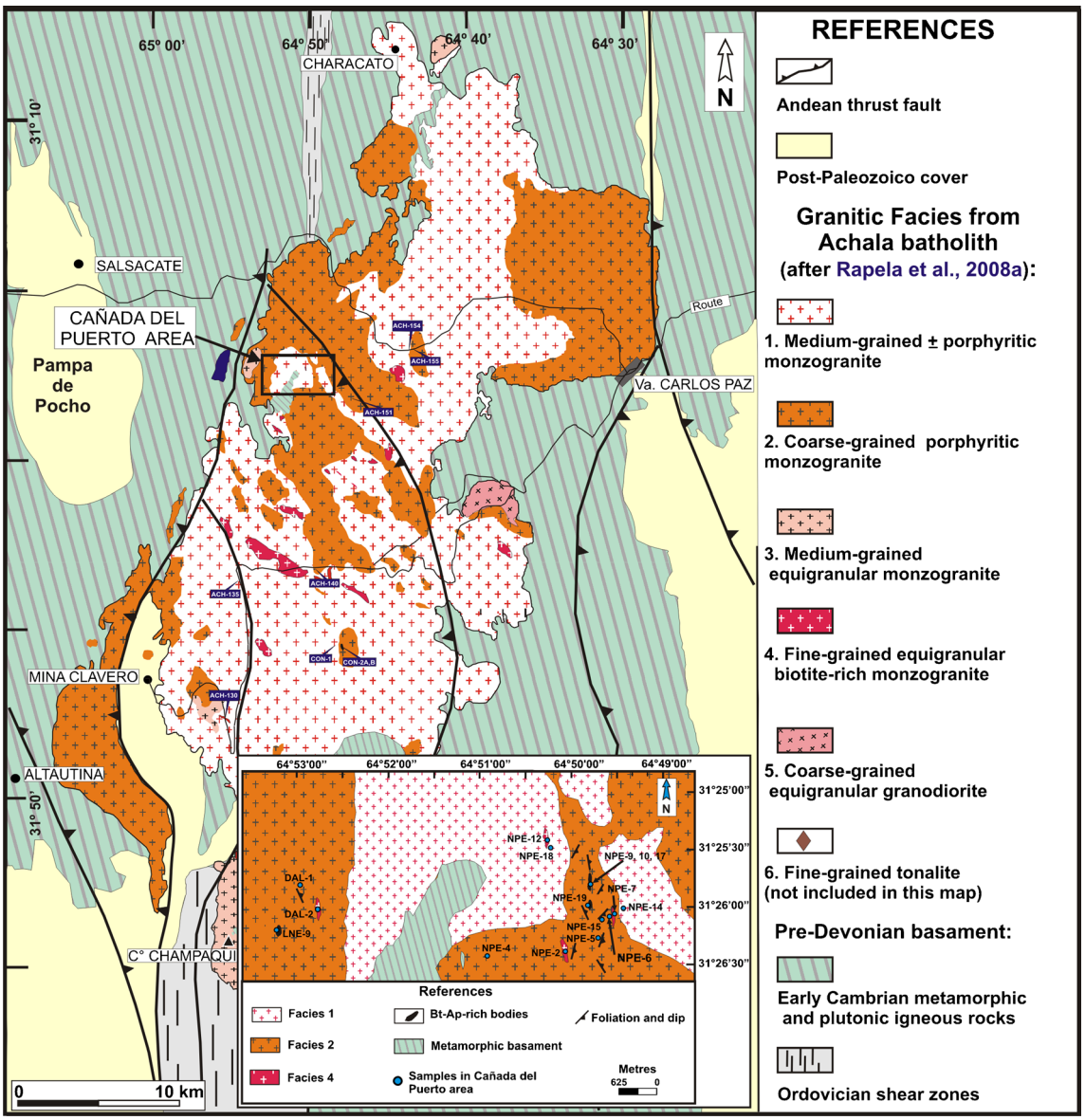

Fig. 2 Geological sketch map of the Late Devonian Achala batholith. The granitic facies are those defined by Rapela et al. (2008b). **Inset:** *rectangle* shows the location of main study area. Studied samples are shown in the figure

Facies 4. Fine-grained, biotite-rich equigranular monzogranite, that forms small (up to about 1.5 km) lenticular bodies, abundant in the central part of the batholith.
Facies 5. Coarse-grained equigranular granodiorite, with a Qtz-Pl-Kfs-Bt-Ms-±Hbl-Ap-Zr-Rt-Ttn-Op mineral association. This facies is restricted to two units identified on the eastern side of the body.
Facies 6. Fine-grained tonalite (Pl-Qtz-Bt±Ms-Ap-Ttn-Zrn-Op), defined in minor intrusive bodies within the porphyritic Facies 1 and 2.

This nomenclature is followed in the present work.

A variety of enclaves have been described from the Achala granites, including diorite and tonalite, mafic microgranular enclaves and unusual biotite-apatite layered enclaves (Dorais et al. 1997) or unusual small-scale biotite-apatite bodies in the porphyritic facies 2. We prefer the term bodies according to the description carried out in Section "Biotite-apatite bodies". Metamorphic xenoliths of the country rocks are ubiquitous.

Mineralization in the batholith was summarized by Lira and Kirschbaum (1990) and includes: (a) Be-P-Nb-Ta pegmatites, (b) feldspathic episyenites, which host uranium minerals (metautunite and metatorbenite) that crystallized from exogenous uraniferous solutions, (c) tungsten deposits occurring as wolframite-bearing quartz veins intruded into either the granite or the country rocks, or as scheelite-bearing calc-silicate skarns. Although fluorite is a rare accessory mineral in the granites, fluorite veins of economic interest are often located close to the contacts with the metamorphic envelope. Some of these veins were formed by hydrothermal circulation of fluids during the Late Jurassic and Early Cretaceous (Galindo et al. 1997).

Pegmatites and aplites are widely distributed in the batholith and in the metamorphic envelope. Galliski (1994) suggested that they are most likely fractionated of A- (+S-) type magmatism.

Largely dominated by 70–74 wt % SiO_2 monzogranites, the batholith has however a wider, 60–76 wt % SiO_2 range, within the fields of the calc-alkalic to alkali-calcic series. The Achala granites have been termed *aluminous A-type* as they are all peraluminous, and typically show enrichments in F, Ga, Nb, high Ga/Al ratios and low K/Rb ratios as does typical A-type granite (Rapela et al. 2008a).

Recently, Dahlquist et al. (2013) have reported Hf and Nd isotope data from the Achala granites suggesting that the magmas were largely derived from the recycling of old crustal rocks. Consistent with this conclusion are the zircon age patterns of porphyritic granites reported by Rapela et al. (2008a), which show inherited components (ca. 660 and 700 Ma) commonly found in the Cambrian metasedimentary country rocks of the batholith which are therefore a likely source component. In addition, metamorphic rim with 540 Ma are recognized in these zircons with ages crystallization of 379 Ma.

Based on significantly more negative values of ε_{Hft} in one granitic sample of the Achala batholith, and the high concentrations of some distinctive elements such as F and P_2O_5, Dahlquist et al. (2013) suggested derivation from older crustal metasediments.

U-Pb zircon crystallization ages from the granitic facies in the central sector of the Achala batholith range from 366±6 to 379±4 Ma (compilation from Rapela et al. 2008a; Dahlquist et al. 2013 and references therein) indicating magmatic emplacement during a relatively short interval in the Late Devonian. These results are consistent with two U-Pb conventional zircon ages of 368±2 Ma obtained from biotite-apatite bodies and the hosted porphyritic granites (Facies 2, see Section Petrology and mineral chemistry of the granitic rocks and biotite-apatite bodies), respectively (Dorais et al. 1997). These ages should be considered with caution because inherited zircon has been reported in recent studies (e.g., Rapela et al. 2008a). However, the field evidence suggests synchronous emplacement (see Section Field occurrence and petrography description) and Nd-isotopes data reveal a common source for granitic rocks and biotite-apatite rich bodies. Further precise geochronological studies are still needed to test if Early Carboniferous rocks are present, for example in the northern part of the batholith, where Rb-Sr isochrons gave ages of 358±9 Ma (Rapela et al. 1991) and 337±2 Ma (Saavedra et al. 1998).

Petrology and mineral chemistry of the granitic rocks and biotite-apatite bodies

Analytical methods

The Cañada del Puerto area was chosen because it includes granitic facies associated with the unusual presence of small-scale biotite-apatite bodies that can be relevant in the understanding of the petrogenesis process as discussed in Section "Petrogenesis of the biotite-apatite bodies: A discussion". In addition, U mineralization was noticed by Lira (1985) in the region studied in this work and thus, the biotite-apatite bodies can have played a role in the preconcentration of U.

Numerous samples were collected from the Cañada del Puerto area, of which 24 were selected for petrographic investigations. Based on these results and our large field observations, we chose representative samples for geochemical, chemical mineral, isotope, and geochronological analysis. Some additional samples with geochemical and geochronological determination were collected outside the La Cañada del Puerto area in previous studies and are reported in this work. The rocks are assigned to the granitic facies described in Table 7.

Major element compositions were determined for three samples using a ThermoARL sequential X-ray fluorescence spectrometer, following the procedure described by Johnson

et al. (1999). Trace element compositions were determined using ICP-MS, following the procedure described in http://www.sees.wsu.edu/Geolab/note/icpms.html. For biotite-apatite samples the high concentration of P_2O_5 in some cases lay beyond the upper limit of the calibration, leading to reduced precision (e.g., P_2O_5 in NPE-17).

Additionally, whole-rock major and trace elements were determined for two representative samples by ICP-OES and ICP-MS (following the procedure 4-Lithoresearch code), at Activation Laboratories, Ontario, Canada (ACTLABS). Following lithium metaborate/tetraborate fusion, samples are dissolved in a weak nitric acid solution. Major elements, Be, Sc, V, Sr, Ba, and Zr are determined by Inductively Couple Plasma – Optical Emission Spectroscopy (ICP-OES). All other trace elements are determined by Inductively Coupled Plasma – Mass Spectrometry (ICP-MS). For major elements precision and accuracy are generally better than 2 % (relative). For trace elements precision and accuracy are generally better than +/− 6 % for all elements present at 10 times above background.

LA-ICP-MS analysis of separated zircons from sample ACH-155 was carried out at the School Earth and Environmental Sciences (SEES) Washington State University (WSU) (Pullman, USA), using a New Wave Nd:YAG UV 213-nm laser coupled to a ThermoFinnigan Element 2 single collector, double-focusing, magnetic sector ICP-MS. Operating procedures and parameters are discussed in greater depth by Gaschnig et al. (2010). Fractionation in the plasma was corrected by normalizing U/Pb and Pb/Pb ratios of the unknowns to those of zircon standards (Chang et al. 2006). For this study we used one zircon standard: Peixe, with an age of 564 Ma (Dickinson and Gehrels 2003).

Sm–Nd analyses of the three representative Bt-Ap rich bodies were carried out at the Geochronology and Isotope Geochemistry Centre of the Complutense University, Madrid, Spain. Whole-rock powders were decomposed in 4 ml HF and 2 ml HNO_3 in Teflon digestion bombs heated for 48 h at 120 °C and finally in 6 M HCl. Sm and Nd were determined by isotope dilution using spikes enriched in ^{149}Sm and ^{150}Nd. Ion exchange techniques were used to separate the elements for isotopic analysis. Sr and REE were separated using Bio-Rad AG50×12 cation exchange resin. Sm and Nd were further separated from the REE group using Bio-beads coated with 10 % HDEHP. Isotopic analyses were made on an automated multicollector VG® SECTOR 54 mass spectrometer. Analytical uncertainties are estimated to be 0.006 % for $^{143}Nd/^{144}Nd$ and 0.1 % $^{147}Sm/^{144}Nd$. Replicate analyses of the La Jolla Nd-isotope standard yielded an average $^{143}Nd/^{144}Nd$ ratio of $^{143}Nd/^{144}Nd=0.511848\pm0.000003$ (2σ) with $n=36$. Errors are quoted throughout as two standard deviations from measured or calculated values.

Mineral chemistry was determined on representative rock samples using two electron microprobes. A JEOL JXA 8500F *Hyperprobe* equipped with 5 tuneable wavelength dispersive spectrometers at the SEES, WSU (Pullman, USA). The beam current was 15 kV, probe current of 20 nA, and the beam diameter was 5 mm. A JEOL JXA-8900-M *Superprobe* equipped with five crystal spectrometers at the Luis Brú Electron Microscopy Center, Complutense University, Madrid, Spain. Absolute abundance for each element was determined by comparison with standards (Jarosewich et al. 1980; McGuire et al. 1992). Operating conditions were: acceleration voltage of 15 kV, probe current of 20 nA, with a beam diameter between 1 and 2 mm. An on-line ZAF program or PhieRhoeZ algorithm (Armstrong 1988) was used with the JEOL JXA 8500F *Hyperprobe* and an on-line ZAF program was used with the JEOL JXA-8900-M *Superprobe*. The data obtained from each electron microprobe are indicated in the Tables containing mineral chemical data. Representative mineral compositions are reported in Tables 1, 2, 3, 4, 5 and 6, while complete data (about 150 analyses) are found in Mineralogy and Petrology **Data Repository**.

Systematic semi-quantitative analysis using JEOL JXA-8230 electron microprobe equipped with an ultra-thin window at Electron Microscopy Laboratory and X-ray Analyses unit of Cordoba National University (http://www.famaf.unc.edu.ar/lamarx/lamerx1sem.html) were carried out to identify accessory minerals in Bt-Ap bodies. Operating conditions were: acceleration voltage of 15 kV and 20 kV.

Modal proportions were obtained on sample NPE-10 from combined modal counting and ImageJ software (Rasband 2011). This software discriminates different grey intensities of the object using JPG images. Five pictures from thin section were analysed, obtaining the following average: Bt=72.2 %, Qtz=9.7 %, Ms=9.2 %, and Ap=8.9 %. Later Qtz was eliminated from the assumed magmatic assemblage (see next

Table 1 Representative composition of alkali feldspar in granitic rocks in Cañada del Puerto area from electron microprobe

Samples	NPE-6 Average $n=16$	NPE-14 Average $n=12$	NPE-12 Average $n=3$
wt. %			
SiO_2	64.28	64.77	64.37
Al_2O_3	19.35	18.74	19.05
CaO	0.04	0.04	0.03
Na_2O	1.48	1.08	1.20
K_2O	14.54	14.85	14.74
Total	99.68	99.28	99.40
Ab	13.83	9.91	11.02
An	0.16	0.20	0.14
Or	86.01	89.89	88.84

In all Tables: Facies 2, porphyritic monzogranite, NPE-6; Facies 1, monzogranite ± Kfs phenocrysts, NPE-14; Facies 4 monzogranite, NPE-12, and biotite-apatite body, NPE-10

Ab Albite, *An* Anortite, *Or* Orthoclase, *bdl* below detection limit

**JEOL JXA 8500F Hyperprobe* and ***JEOL JXA 8900 Superprobe*. Details in Mineralogy and Petrology Data Repository

Table 2 Representative composition of plagioclase in granitic rocks in Cañada del Puerto area from electron microprobe

Sample	NPE-6									Average[1]	Average	Average	NPE-14	NPE-12
Analysis number	Pl_b 359core**	Pl_a	Pl_b	Pl_b inclusion	Pl_a 367late rim**	Pl_a 15core*	Pl_a 17rim*	Pl_b 370core(inc)**	Pl_b 371rim(inc)**	Pl_a	Pl_b	Pl_b inclusion	Average $n=7$	Average $n=6$
wt. %														
SiO_2	62.39	62.51	63.33	63.26	66.73	62.90	63.53	63.77	64.29	63.43	62.45	64.03	65.43	63.68
Al_2O_3	22.64	22.39	23.30	23.36	21.10	22.26	21.68	22.32	22.49	22.49	22.52	22.41	21.85	22.12
CaO	3.04	3.02	3.50	3.59	1.22	2.86	2.43	2.70	2.80	2.97	3.03	2.75	2.18	2.52
Na_2O	10.94	11.14	9.12	9.50	10.75	9.79	10.54	10.89	10.92	9.83	11.04	10.91	10.31	10.4
K_2O	0.16	0.15	0.30	0.28	0.14	0.29	0.15	0.17	0.12	0.23	0.16	0.15	0.22	0.2
Total	99.17	99.21	99.55	99.98	99.94	98.10	98.33	99.85	100.62	98.94	99.19	100.24	99.64	98.92
Ab	85.96	86.32	81.06	81.42	93.36	84.58	87.98	87.17	87.05	84.59	86.11	87.08	88.49	87.2
An	13.20	12.92	17.18	17.00	5.85	13.66	11.20	11.95	12.32	14.12	13.06	12.13	10.28	11.68
Or	0.84	0.76	1.76	1.58	0.79	1.66	0.82	0.89	0.63	1.29	0.83	0.79	1.23	1.12

Ab Albite, *An* Anortite, *Or* Orthoclase. *Inc* inclusion in Kfs

[1] Average excluding the sample 367

**JEOL JXA 8500F Hyperprobe* and ***JEOL JXA 8900 Superprobe*

Table 3 Representative composition of biotite in granitic rocks and biotite-apatite bodies in Cañada del Puerto area from electron microprobe

Samples	NPE-6 Average $n=19$	NPE-14 Average $n=10$	NPE-12 Average $n=10$	NPE-10 Average $n=14$
wt. %				
SiO_2	35.16	35.96	34.01	34.39
TiO_2	2.45	2.33	2.55	2.19
Al_2O_3	18.10	16.95	18.21	17.78
FeO	21.29	21.62	22.77	21.81
MnO	0.48	0.33	0.62	0.38
MgO	6.96	7.54	5.81	7.19
CaO	0.02	0.03	0.03	0.02
Na_2O	0.11	0.06	0.12	0.18
K_2O	9.48	9.40	9.15	9.37
F	1.50	1.12	0.94	1.69
Total	95.55	95.34	94.21	94.99
F=O	0.63	0.47	0.40	0.71
CTotal	94.92	94.87	93.81	94.28
FeO/MgO	3.06	2.87	3.97	3.04
Structural formulae calculated on basis 22 O				
Al^{IV}	2.51	2.39	2.39	2.56
$Fe^{2+}/(Fe^{2+}+Mg)$	0.63	0.62	0.62	0.63

Total iron expressed as FeO. *bdl* below detection limit

Section), yielding a magmatic assemblage (modal %) of Bt=80 %, Ms=10 % and Ap=10 %.

Field occurrence and petrography description

Our study was carried out on representative rocks of the Achala batholith in the La Cañada del Puerto area (Fig. 2).

Table 4 Representative composition of apatite in granitic rocks and biotite-apatite bodies in Cañada del Puerto area from electron microprobe

Samples	NPE-6 Average $n=4$	NPE-14 Average $n=7$	NPE-12 Average $n=8$	NPE-10 Average $n=9$
wt. %				
SiO_2	bdl	bdl	0.05	0.03
TiO_2	0.05	bdl	0.03	0.02
Al_2O_3	0.01	0.01	0.02	0.02
Fe_2O_3	0.37	0.16	0.26	0.59
MnO	0.97	0.31	0.95	1.51
MgO	0.01	bdl	bdl	0.01
CaO	53.94	54.82	54.49	52.90
P_2O_5	42.33	42.20	42.23	42.04
F	3.61	3.35	3.73	3.71
Total	101.24	100.86	101.69	100.77
F=O	1.52	1.41	1.57	1.56
CTotal	99.72	99.45	100.12	99.21

Total iron as Fe_2O_3

bdl below detection limit

All data from *JEOL JXA 8900 Superprobe*

Based on petrological and geochemical data, three main granitic facies were recognized: facies 1, 2, and 4 of Rapela et al. (2008a) defined in Section "Geology of the Achala batholith". As already stated, facies 1 and 2 are by far the most abundant in Achala batholith. Additionally, one subordinate rock type named here as biotite-rich granite was recognized in the area (composition in Table 7). This forms a tabular small-scale outcrop emplaced in facies 2; according to Zarco (2006) it was emplaced in a fracture generated during the development of magmatic shear. The observed contact between facies is

Table 5 Representative composition of oxides in granitic rocks and biotite-apatite bodies in Cañada del Puerto area from electron microprobe

Samples	NPE-6		NPE-14	NPE-12	NPE-10
	345	358	Average $n=6$	Average $n=5$	Average $n=9$
wt%					
SiO_2	0.46	3.28	0.05	bdl	0.38
TiO_2	96.91	51.23	50.76	48.56	21.63
Al_2O_3	0.28	0.25	0.04	0.07	0.16
FeO	0.83	28.76	43.48	36.59	66.21
Fe_2O_3	0.92	31.95		40.65	73.59
MnO	0.03	9.54	4.37	6.65	0.31
MgO	0.09	0.15	0.02	bdl	0.02
CaO	0.02	0.10	0.03	0.01	0.02
Total	98.71	96.50	98.74	95.94	96.10

In those cases where the Total is low the total iron is expressed as ferric

Table 6 Representative composition of muscovite in granitic rocks and biotite-apatite bodies in Cañada del Puerto area from electron microprobe

Samples	NPE-6 Average $n=10$	NPE-14 Average $n=9$	NPE-12 Average $n=8$	NPE-10 Average $n=14$
wt. %				
SiO_2	45.57	45.61	44.62	44.99
TiO_2	0.97	0.97	0.82	0.80
Al_2O_3	32.93	32.16	33.35	32.39
FeO	2.75	3.94	2.72	3.52
MnO	0.03	0.03	bdl	0.04
MgO	0.90	1.01	0.76	1.06
CaO	0.02	0.02	0.09	0.02
Na_2O	0.44	0.46	0.50	0.61
K_2O	10.32	10.34	10.39	10.23
F	0.55	0.47	0.36	0.55
Total	94.48	94.99	93.53	94.18
F=O	0.23	0.20	0.15	0.23
CTotal	94.25	94.79	93.38	93.95
Structural formulae calculated on basis 22 O				
$Fe^{2+}/(Fe^{2+}+Mg)$	0.63	0.69	0.67	0.65

Total iron expressed as FeO. *bdl* below detection limit

sharp, facies 4 form small-scale bodies emplaced in facies 1 and 2 suggesting a late intrusion.

Biotite-apatite bodies are also hosted in facies 2, exhibit sharp contacts, and occur as elongated, tabular or drop-like bodies ranging from few to tens of metres in length with thicknesses of up to 1 metre.

Petrography and chemistry are considered in the next sections for each facies separately; data for muscovite in the three facies and biotite-apatite bodies are considered later in Section "Origin of the muscovite in the granitic rocks".

Facies 1: Medium-grained ± porphyritic monzogranite

Facies 1 is widespread in the studied area (Fig. 2). It is a massive equigranular medium-grained (ca. 0.5 cm), mica-rich monzogranite (Fig. 3c) with erratic presence of alkali feldspar phenocrysts. Contact with facies 2 is irregular and sharp. Petrography studies reveal that the modal magmatic assemblage is Pl (27 %), Kfs (24 %), Qtz (34 %), Bt (7 %), Ms (6 %) with scarce apatite and oxides as accessory minerals.

Alkali feldspar is microcline with medium-grained, ranging from 3.5×3 mm to 2×1 mm, and forms tabular subhedral–anhedral crystals, generally with perthitic texture. The representative composition of microcline ranges from $Or_{86.9}$ to $Or_{92.7}$ and the complete composition can be observed in Table 1.

The plagioclase is medium-grained, ranging from 3×1.3 mm to 2×0.7 mm, forming tabular and anhedral crystals with polysynthetic twinning. Its composition ranges from oligoclase $An_{15.9}$ in the core to albite $An_{6.6}$ in the rim (Table 2).

Biotite is medium-grained (1.5×0.8 mm) evenly distributed throughout the rock. It occurs as light to dark brown subhedral plates or irregular sections, with inclusions of Ap and Zrn. In terms of Al^{IV} vs. $Fe^{2+}/(Fe^{2+}+Mg)$ the biotites show relatively high siderophyllite–eastonite (average Al^{IV}= 2.39 atom/formula unit, Table 3) together with high F contents (average F=1.12, $n=10$ Table 3). Fluorapatite (ca. 0.5 %, with F=3.35, $n=7$, Table 4) is euhedral to subhedral with dominant hexagonal and short prismatic forms. It is variably fine-grained, 0.2 to 0.4 mm, and is commonly observed as an inclusion in biotite or muscovite. This rock contains Qtz and ilmenite (ca. 0.4 %) is the oxide mineral (Table 5). Systematic analysis using the electron microprobe (determining Zr and LREE data) reveals the presence of two radioactive minerals, zircon and monazite.

Facies 2: Coarse-grained porphyriticmonzogranite

In the studied area, the dominant granitic rock type is porphyritic monzogranite, where alkali feldspar phenocrysts (mostly 1.0−1.5×0.6−1.0 cm) are enclosed in a medium- to coarse-grained (0.5 – 0.8 cm) matrix of biotite, alkali feldspar, quartz and plagioclase (Fig. 3a).

A fabric defined by the alignment of alkali feldspar phenocrysts is developed in some rocks of this facies and is interpreted as magmatic in origin. The orientation of phenocrysts is variable, but mainly between 50° and 325°. In some locations, the granite is intruded by (i) equigranular fine-grained (< 1 cm) biotite monzogranite dykes (1.0–1.5 m in thickness) with an orientation of 30°/60°E and (ii) a foliated biotite-rich granite type (NPE-5) commonly occurring in NNW-SSE elongate tabular bodies (Figs. 2 and 3b).

Petrography studies from porphyritic monzogranite reveal that the modal magmatic assemblage is Pl (33 %), Kfs (32 %),

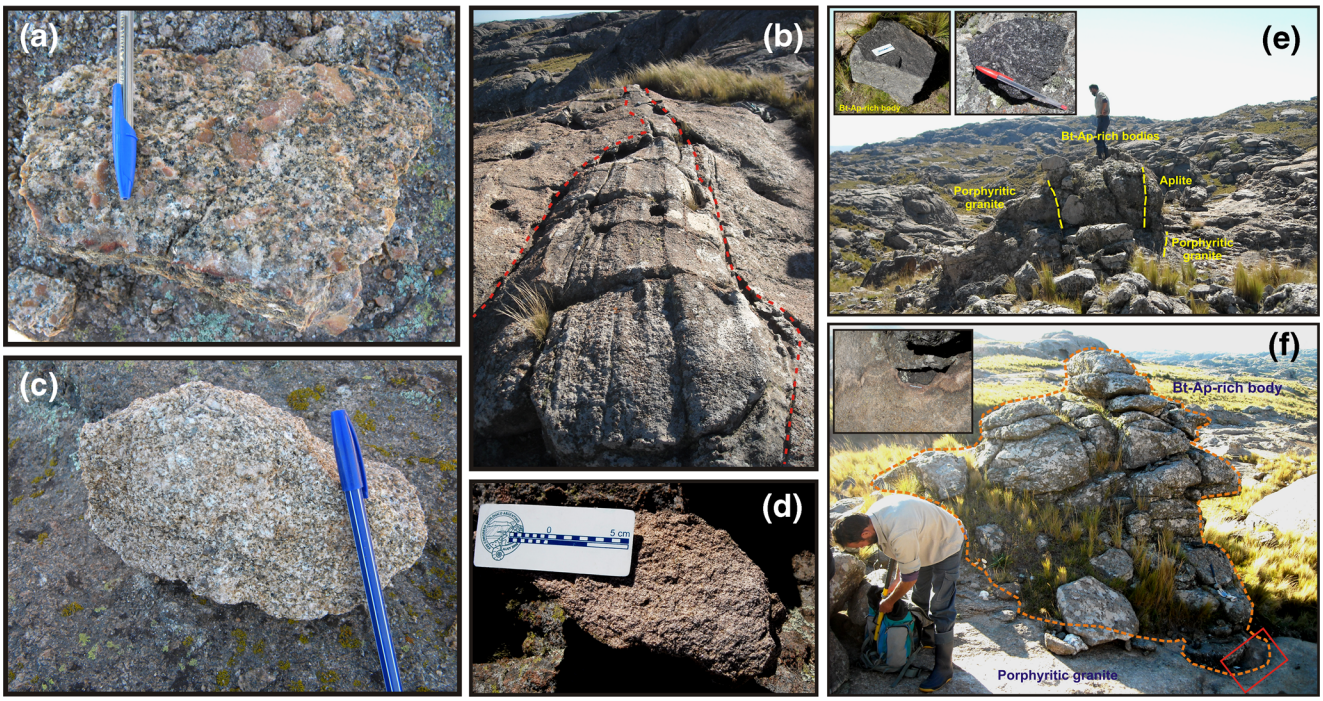

Fig. 3 Field characteristics of the granitic rocks and biotite-apatite bodies in the Cañada del Puerto area. **Granitic rocks**: (**a**) Facies 1, equigranular ± porphyritic monzogranite, (**b**) biotite-rich monzogranite emplaced in facies 2. The discontinuous red line indicates body boundary. Foliation: 20°/85°E, (**c**) Facies 2, porphyritic monzogranite, and (**d**) Facies 4, equigranular monozogranite. The dominant morphology of **biotite-apatite bodies** housed in porphyritic monzogranite: (**e**) tabular form (150 m × 1.5 m approximately, sample NPE-10) and (**f**) drop-like bodies (ca. 1.8 m diameter, sample NPE-17). Representative texture of biotite-apatite bodies in inset of Fig. 3e. The biotite-apatite bodies are housed in porphyritic monzogranite with sharp and lobule contacts (see inset in Fig. 3f, g). **g** Unusual disrupted biotite-apatite body (sample CON-2A, 2B). Also are observed mafic microgranular enclaves (light grey) that are identified in the photograph with MME. **h** Lenses inclusions of quartz and vein of Kfs in sample NPE-10 (wide 1 cm). Photographs (**i**) and (**j**) from rectangles in photograph (**g**). (**i**) and (**j**) Phenocrysts of K-feldspar in biotite-apatite bodies: (**i**) unorientated alkali feldspar phenocrysts transferred from the hosted porphyritic granitic rocks. *Arrows* indicate K-feldspar phenocrysts (samples CON-2A, 2B). **j** Oriented K-feldspar phenocrysts transferred from the hosted porphyritic granitic rocks (left). Red arrows indicate K-feldspar phenocrysts orientation. Vein of Kfs are also observed. Sample LNE-9 is a drop-like body. Inset in (**j**) is a demolished block from LNE-9. **k** Repetitive layering formed by biotite and granitic material. **l** biotite-apatite bodies forming dykes with K-feldspar phenocrsyst transferred from the host granite which are concentrated in the centre of dyke increasing its size. K-feldspar phenocryst are oriented on the wall of the dyke (see inset). **m** Photomicrographs of typical minerals of the biotite-apatite bodies in the Cañada del Puerto area (NPE-10). Biotite, apatite, and zircon define the magmatic minerals assemblage that forms this unusual rock

Qtz (25 %), Bt (7 %), Ms (3 %) with apatite and oxides as accessory minerals. Alkali feldspar is microcline. In thin section this mineral has typical medium to coarse grain-size (ranging from 3.3×2.2 mm to 6.5×4 mm), and forms tabular subhedral–anhedral crystals, generally with perthitic texture and inclusions of plagioclase and minor quartz and muscovite. The representative composition of microcline ranges from $Or_{81.7}$ to $Or_{90.4}$, and the complete composition is reported in Table 1.

Two main varieties of plagioclase were recognized: (a) medium-grained (Pl_a, 2.2×1.0 mm, 1.5×1.0 mm), tabular and anhedral crystals and (b) fine-grained (Pl_b, 1.0×0.3 mm), tabular, subhedral crystals with polysynthetic twinning. Pl_a is scarce whereas Pl_b occurs in the matrix or as inclusion in microcline. Both plagioclases have uniform oligoclase compositions of $An_{17.1}$ for Pl_a and $An_{12.6}$ for Pl_b. Complete compositional data is reported in Table 2.

Biotite is the only mafic mineral. It is medium-grained, ranging from 1.8×1.4 mm to 1.4×0.4 mm. All biotites form subhedral laths or irregular sections and exhibit pleochroism from light to dark brown. Ap and Zrn occur as inclusions in biotite, the Zrn producing strong pleochroic halos. In terms of Al^{IV} vs. $Fe^{2+}/(Fe^{2+}+Mg)$ the biotites show high siderophyllite–eastonite contents (Table 3). They have relatively high Al^{IV} (average 2.51 atom/formula unit) together with very high and distinctive F contents (average F=1.50 %, Table 3). Biotites with high Al^{IV} (> 2.50 approximately) seem to be characteristic of peraluminous magma (e.g., Dahlquist et al. 2005a, 2007; Clarke et al. 2005 and references therein).

These porphyritic monzogranites contain quartz, a low content of apatite and oxides (ca. 0.3 %). The apatite is fine-grained, ranging from 0.1 to 0.7 mm in diameter and is fluorapatite in composition (F=3.61 %, n=4 Table 4). Oxides are ilmenite and rutile (Table 5). Electron microprobe analysis (including Zr and LREE data) indicates the presence of two radioactive minerals, zircon and monazite.

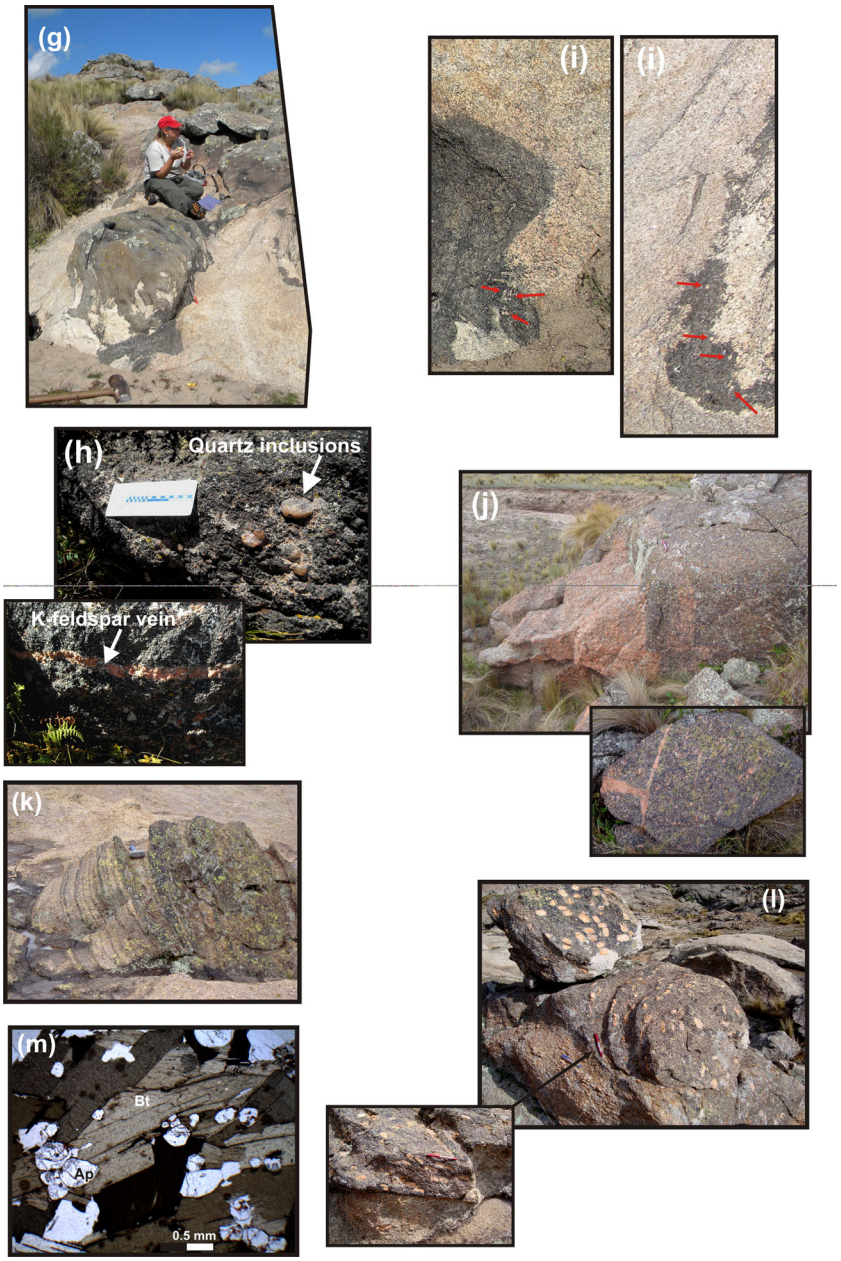

Fig. 3 (continued)

Facies 4: fine-grained equigranular biotite-rich monzogranite

This granitic rock type is equigranular medium-grained (ca. 0.3 cm) and massive, with K-feldspar phenocrysts absent (Fig. 3d). This facies forms small-scale bodies with sharp contacts, defining elongated and tabular bodies with thicknesses ranging from 0.5 m to 20 metres emplaced in facies 1 and 2, respectively (Fig. 2). Petrographic investigations reveal a modal magmatic assemblage of Pl (30 %), Kfs (29 %), Qtz (30 %), Bt (6 %), Ms (5 %) and oxides and low modal proportion of Ap as accessory minerals.

Alkali feldspar is microcline. This mineral has medium-grained (Mc_a, 2.5×2 mm), and forms tabular subhedral–anhedral crystals, generally with perthitic texture. The representative composition of microcline (ranging from $Or_{81.7}$ to $Or_{90.4}$) is shown in Table 1.

The plagioclase is fine-grained, ranging from 0.3×0.7 mm to 0.5×0.8 mm, forming tabular and anhedral crystals with polysynthetic twinning, and is confined to the matrix. Its composition ranges from $An_{14.9}$ in the core to $An_{7.2}$ in the rim (oligoclase to albite, Table 2).

Biotite is the only mafic mineral. Grain-size is variable, ranging from 0.3×0.8 mm to 0.8×1.4 mm. Biotite forms subhedral laths or irregular sections and exhibit pleochroism

from light to dark brown. Ap and Zrn are common inclusions. In terms of Al^{IV} vs. $Fe^{2+}/(Fe^{2+}+Mg)$ the biotites show high siderophyllite–eastonite (average Al^{IV}=2.59 atom/formula unit, Table 3) together with high F contents (average F= 0.94, n=10 Table 3).

This rock contains quartz, low percentages of fluorapatite (ca. 0.1 %, with F=3.73, n=8, Table 4), and oxides (ca. 0.2 %). Fluorapatite is euhedral to subhedral with dominant hexagonal and short prismatic forms. It is variably fine-grained, ranging from 0.2 to 0.5 mm in diameter and is commonly observed as inclusions in biotite. Ilmenite is the oxide in this rock (Table 5). Systematic analysis using the electron microprobe (including Zr and LREE data) reveals the presence of two radioactive minerals, dominant zircon and monazite.

Biotite-apatite bodies

In the Cañada del Puerto area the small-scale biotite-apatite bodies are hosted in the porphyritic monzogranites (facies 2), with sharp and lobed contacts, defining elongated, tabular or drop-like bodies ranging from a few to dozens of metres in length with thicknesses of up to 1 metre (Fig. 3e, f). NPE-10 is from an elongated tabular body, NPE-9 and LNE-9 define drop-like bodies, and CON-2A, B form unusual disrupted body (Fig. 3e, f, g; sample location in Fig. 2). These bodies can be cut by centimetric lenses, veins or inclusions of quartz or K-feldspar (Fig. 3h). Remarkably, biotite-apatite bodies are included in granitic facies 2 and display a distinctive response in the scintillometer (between 1,000 – 5,000 counts/second).

Repetitive layering formed by biotite and granitic material is another magmatic structure commonly observed (Fig. 3k).

The field evidence shows that alkali feldspar phenocrysts were transferred from the host porphyritic granitic rocks (Fig. 3i, j). In particular, the dyke-like biotite-apatite bodies show K-feldspar phenocrysts transferred from the host granite which are concentrated in the centre of dyke and increasing in size (Fig. 3l).

Petrography of these mafic bodies reveals igneous textures, with a magmatic assemblage of biotite (80 %), muscovite (10 %), and apatite (10 %) with zircon, monazite, and scarce oxides as accessory minerals (Fig. 3m).

Biotite is far the most abundant mineral, varying from coarse-grained (Bt_a, 5×1.2 mm, the dominant type) to medium-grained (Bt_b, 2.0×0.2 mm). All biotite forms subhedral tabular or irregular sections, and has light to dark brown pleochroism. Commonly, biotite forms large clusters, where apatite, zircon, monazite and oxides occur as inclusions. Zircon and monazite produce strong pleochroic halos. In terms of Al^{IV} vs. $Fe^{2+}/(Fe^{2+}+Mg)$ the biotites show high siderophyllite–eastonite (average Al^{IV}=2.56 atom/formula unit, Table 3)contents, together with high F (average F= 1.69). Compositionally, they show similarities with the biotite in facies 1, 2, and 4 (see Table 3).

Fluorapatite is also an abundant mineral, euhedral to subhedral with dominantly hexagonal and short prismatic forms. It has variable size, ranging from medium- (1.2 mm of diameter) to fine-grained (0.2 mm of diameter), and is commonly observed as an inclusion in biotite. These apatites have relatively high F contents (F=3.74 % and CaO=52.76 %; average from 9 samples, Table 4).

Quartz was also observed in the rock, commonly medium-grained (2.0–2.5 mm in diameter), but sometimes fine-grained (0.2 mm in diameter). Veins formed by coarse-grained quartz strongly suggest a later origin, filling interstices or fractures.

Systematic analysis using the electron microprobe (determining Zr and LREE data) indicate the presence of two radioactive minerals, zircon and monazite; magnetite and ilmenite are the oxides in this rock (Table 5). In addition, systematic semi-quantitative analysis reveals very high modal proportion of monazite. A single xenotime crystal was founded.

Origin of the muscovite in the granitic rocks

Muscovite is the other sheet silicate present in all studied rocks, with an average modal proportion (%) of 2.8, 6.4, 5.1, and 10 for facies 1, 2, 4, and biotite-apatite bodies respectively. Care was taken to determine whether it is of primary or secondary origin, since primary white mica is widely held to be an indicator of peraluminous magmas (Speer 1984). Miller et al. (1981) describe petrographic criteria for determining whether white mica is primary or secondary, including (1) coarse grain size, comparable to other primary magmatic phases, (2) subhedral or euhedral form, (3) enclosure by any mineral from which the mica may have formed through alteration, and (4) presence in a rock with clean, unaltered, igneous texture. Our observations using these criteria suggest that both types are present in these rocks. The inferred primary muscovites form individual unaltered coarse grain-size and are dominantly subhedral.

Chemical data for muscovite are taken to represent a robust discriminant and have been used by several authors to clarify its origin (e.g., Dahlquist et al. 2005a and references therein). Chemical analyses (Table 6) from assumed primary muscovite in the three granitic facies and biotite-apatite bodies fall in the primary muscovite field of the Mg–Ti–Na diagram (Fig. 4) as established by Miller et al. (1981) and strongly suggest a magmatic origin for muscovite. This is consistent with previous conclusions reported by Dorais et al. (1997).

Whole-rock geochemistry of the granitic rocks and biotite-apatite bodies

Major- and trace-element compositions of 19 representative samples from the Cañada del Puerto area were collected. In addition, six whole-rock analyses of the central part of the Achala batholith, assignable to the granitic facies previously

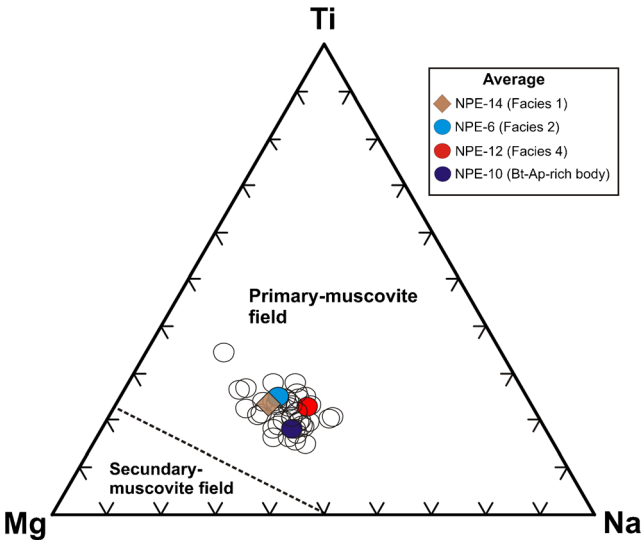

Fig. 4 Projected composition of white micas in the triangular diagram Mg–Ti–Na (data in Table 6). The limit between fields for secondary and primary micas is from Miller et al. (1981)

described in Section "Petrology and mineral chemistry of the granitic rocks and biotite-apatite bodies", were also included to give a wider whole-rock geochemistry data base (sample locations, lithology, and geochemical data are detailed in Table 7 and Fig. 2).

Major elements

The data show that the granitic rocks are monzogranites, and their SiO_2 content varies within a restricted range from 69.8 to 74.5 wt.% (Table 7). Facies 4 has the highest SiO_2 content (72.1–74.5 %).

On the alkalis vs. silica classification diagram of Wilson (1989), the rocks plot dominantly at the silica-rich end of the field of alkaline granites, with transition to the subalkaline granites (monzogranite) field (Fig. 5).

The granitic rocks are peraluminous (aluminium saturation index, ASI=1.10–1.40) and have a relatively high agpaitic index (AI=0.65–0.78, average=0.72) (Fig. 6 and Table 7). The monzogranites are poor in CaO (0.46–1.53, average=0.88 wt.%) and extremely rich in FeO^t, with high $FeO^t/(FeO^t+MgO)$ ratios (0.78–0.88, average=0.82).

They are also enriched in MgO relative to TiO_2 ($MgO/TiO_2 > 1$) and are moderately enriched in total alkalis (7.20–8.90 wt.%), with relatively high K_2O contents (K_2O/Na_2O= 1.20–2.21). The granitic rocks generally follow the alkali-calcic and ferroan trend on the Na_2O+K_2O–CaO and $FeO^t/(FeO^t+MgO)$ vs. SiO_2 diagrams of Frost et al. (2001) (Fig. 7a, b).

Biotite-apatite bodies samples were collected trying to exclude the presence of quartz and K-feldspar considering the assumed magmatic assemblage (see Facies 2: Porphyritic monzogranite Section). In agreement with their mineral assemblage the biotite-apatite bodies have an unusual geochemistry composition, distinguished by very low SiO_2 contents, ranging from 32.83 to 50.26 SiO_2 wt.%, low Na_2O, high TiO_2, FeO^t, MnO, MgO, CaO, K_2O and very high P_2O_5 contents (Table 7). The summed analyses are low, ranging from 92.71 to 95.52 wt.%. The referred low total could be explained by the high modal proportion of biotite (80 % of biotite with $H_2O \sim 3$ – 4 wt%, F=1.70 %, Table 3) plus muscovite (10 % of muscovite with $H_2O \sim 4$ wt%, with F=0.55 wt%, Table 6), and apatite (10 % of apatite with F=3.71 wt%, Table 4).

Trace elements and REE

The granitoids have concentrations of high-field-strength elements (HSFE: Y, Nb, Ga, Ta, U, Th, LREE, etc.) comparable to those reported for anorogenic granitic complexes, such as the A-type granites of the Lachlan Fold Belt in Australia, the Hercynian A-type granites of the Kokshaal range in Kyrgyzstan (Table 7), or other A-type granites in the Sierras Pampeanas of Argentina (see data in Table 1 from Dahlquist et al. 2010). Primitive-mantle-normalized spider diagrams show marked negative Ba, Nb, Sr, P, Eu and Ti anomalies and significant enrichment in Rb, Th, U, and Pb (Fig. 8). Rare earth element (REE) abundances vary from 60 to 452 ppm with light REE (LREE) enrichment, significant negative Eu anomalies and negatively sloping HREE patterns (Fig. 8). These patterns are similar to those of some A-type granites reported by Scheepers (2000) and Konopelko et al. (2007, Fig. 7b). Granitic facies 4 is impoverished in REE compared to facies 1 and 2.

The apatite-biotite bodies are strongly enriched in REE (ranging from 1,443 to 4,492 ppm) and HSFE, but with REE patterns very similar to those of the granitic rocks (Fig. 8). Primitive-mantle-normalized spider diagrams are also similar to those of the granitic rocks, with exception of Ba, K, and Sr, due to the absence of feldspar in the magmatic assemblage (Fig. 8). The apatite-biotite bodies are strongly enriched in trace elements that are clearly attributed to the high modal proportions of accessory minerals such as apatite, zircon and monazite, the latter being by far the most abundant.

Geochronological data and isotope geochemistry of the Achala batholith

In order to corroborate the previous ages (see summary in Geological Setting) obtained from Achala granitic rocks, one U-Pb LA-ICPM zircon age is reported here from sample ACH-155 (sample location and chemical composition in Fig. 2 and Table 7, geochronological data in Table 8). The zircons from ACH-155 are mostly elongate grains with subhedral to euhedral-terminations. The SEM-CL images reveal a complex internal structure, mostly with highly luminescent cores (sometimes with a small non-luminescent, possibly xenocrystic centre), surrounded by low-luminescence rims. The

Table 7 Major and trace element data for the studied rocks in Cañada del Puertoand central area of Achala batholith

	Central area Achala batholith					
Granitic Facies	1	1	1	2	2	4
Samples	ACH-140*	ACH-151*	ACH-155*	ACH-135*	ACH-154*	ACH-130*
Latitude (S)	31°36′36.90″	31°26′31.60″	31°23′44.90″	31°37′13.60″	31°23′44.90″	31°45′25.00″
Longitude (W)	64°49′48.50″	64°47′5.70″	64°43′55.60″	64°54′39.80″	64°43′55.60″	64°55′34.40″
wt. %						
SiO_2	73.07	72.16	72.66	70.86	69.75	72.52
TiO_2	0.22	0.31	0.35	0.42	0.55	0.17
Al_2O_3	14.11	14.48	14.38	14.22	14.88	14.31
$Fe_2O_3^t$	2.08	2.25	2.72	3.06	2.91	2.00
FeO^t						
MnO	0.04	0.04	0.08	0.05	0.05	0.05
MgO	0.39	0.43	0.56	0.47	0.75	0.29
CaO	0.93	0.71	1.05	1.53	1.32	0.62
Na_2O	2.71	2.52	2.96	2.88	2.68	3.31
K_2O	5.32	5.57	4.74	5.41	5.07	5.30
P_2O_5	0.28	0.33	0.29	0.17	0.30	0.25
LOI (%)	0.60	0.91	0.79	0.41	0.83	0.73
Total	99.76	99.71	100.57	99.48	99.08	99.55
ppm						
Cs	12.3	10.4	19.9	7	11.1	8.7
Rb	330	486	473	281	414	396
Sr	68	75	86	133	119	51
Ba	175	283	302	721	533	180
La	24.5	41.1	48.6	45.0	90.2	21.4
Ce	55.3	94.2	114	100	218	46.8
Pr	7.05	12.2	14.6	12.7	28.5	6.07
Nd	24	40.9	47.8	42.7	85.1	22.7
Sm	5.07	8.20	9.19	8.61	14.3	5.29
Eu	0.50	0.72	0.77	1.12	1.37	0.43
Gd	4.02	5.36	5.42	6.65	6.93	5.08
Tb	0.70	0.75	0.72	1.01	0.80	0.97
Dy	3.88	3.63	3.53	5.26	3.51	5.78
Ho	0.67	0.57	0.56	0.84	0.55	0.97
Er	1.82	1.4	1.45	1.9	1.36	2.57
Tm	0.26	0.18	0.21	0.22	0.19	0.37
Yb	1.6	1.01	1.32	1.25	1.10	2.27
Lu	0.21	0.14	0.20	0.19	0.15	0.30
U	5.42	22.7	4.17	5.05	4.18	5.48
Th	18.5	35.2	42.2	12.3	74	15.6

Table 7 (continued)

Y	19.5	16.0	16.1	21.4	15.2	30.0				
Nb	20.2	33.7	36.3	20.8	16.9	25.4				
Zr	146	175	203	406	353	117				
Hf	4.3	5.2	5.9	10.8	9.5	3.8				
Ta	1.57	2.3	10.2	4.76	1.58	4.6				
Ga	23	24	23	23	26	22				
Alppm	74674	76632	76103	75256	78749	75732				
ASI	1.26	1.36	1.28	1.10	1.28	1.22				
AI	0.72	0.70	0.70	0.74	0.67	0.78				
M	1.22	1.15	1.21	1.40	1.24	1.25				
T_{Zr}*(°C)*	792	813	822	874	874	770				
Cañada del Puerto area										
1	1	1	2	2	2	2	4	4	4	4
NPE-18**	NPE-14**	CON-1	DAL-1**	NPE-4**	NPE-6**	NPE-15**	DAL-2**	NPE-12**	NPE-7**	NPE-2**
31°25′29.3″	31°26′2.1″	31° 40′ 46.3”	31°25′49.9″	31°26′23.8″	31°26′5.7″	31°26′6.2″	31°26′4.3″	31°25′25.5″	31°26′5.7″	31°26′23.4″
64°50′15.5″	64°49′28.9″	64° 48’ 13.6”	64°52′59.7″	64°50′55.6″	64°49′35.8″	64°49′36.5″	64°52′48.8″	64°50′24.0″	64°49′35.8″	64°50′5.2″
70.98	70.98	71.69	69.16	71.08	71.10	71.18	72.14	73.01	74.49	73.64
0.38	0.36	0.36	0.49	0.22	0.29	0.30	0.18	0.13	0.21	0.12
14.72	14.78	14.50	15.14	15.03	14.73	14.83	14.38	14.32	14.05	14.18
0.25	2.00	1.93	3.24	1.51	1.85	2.04	1.42	1.03	1.36	1.05
0.05	0.04	0.03	0.13	0.04	0.05	0.06	0.07	0.06	0.02	0.07
0.53	0.50	0.59	0.74	0.35	0.47	0.50	0.29	0.15	0.24	0.15
0.73	0.71	1.47	1.08	0.59	0.75	0.79	0.57	0.52	0.72	0.46
2.91	3.07	3.19	3.62	3.08	3.14	3.13	3.17	3.29	3.19	3.23
5.54	5.40	4.49	4.33	5.82	5.51	5.22	5.07	4.72	4.01	4.74
0.41	0.30	0.21	0.43	0.24	0.33	0.34	0.28	0.33	0.26	0.28
1.08	1.09	0.79	0.88	0.95	0.84	1.07	0.90	1.06	1.12	1.07
99.56	99.23	99.25	99.24	98.91	99.06	99.46	98.48	98.61	99.67	98.99
11.1	9.5	9.1	33.2	21.3	8.16	12.2	23.4	17.4	9.49	17.1
402	346	265	551	458	430	445	471	502	291	497
59	82	149	66	62	89	84	50	30	42	30
266	334.1	431	154.7	228	372	322	137	96.5	75	104
65.5	54.6	57.6	59.1	35.5	45.2	47.2	17.5	12.7	10.7	10.4
159	133	123	133	79.5	102	108	37.9	29.8	24.4	24.9
19.6	16.4	14.6	16.2	9.67	12.7	13.5	4.70	3.60	3.11	3.17
74.4	61.8	52.8	59.5	35.16	47.3	49.9	16.91	13.6	11.48	11.87
14.5	11.9	9.14	12.3	7.73	9.98	10.6	3.91	2.90	3.05	2.47
0.95	1.00	1.14	0.8	0.60	0.84	0.82	0.39	0.30	0.33	0.24
8.92	7.00	5.13	9	5.63	7.14	7.47	3.24	2.00	2.85	1.69
1.17	0.90	0.62	1.4	0.91	1.04	1.09	0.58	0.40	0.60	0.28

Table 7 (continued)

5.61	4.30	2.89	7.5	4.90	5.24	5.64	3.43	2.20	4.10	1.74
0.90	0.70	0.47	1.3	0.88	0.86	0.92	0.63	0.40	0.83	0.33
2.17	1.60	1.10	3.2	2.32	2.09	2.21	1.73	1.20	2.41	0.95
0.31	0.20	0.14	0.5	0.34	0.29	0.30	0.27	0.20	0.39	0.16
1.90	1.30	0.83	2.9	2.05	1.66	1.78	1.70	1.30	2.44	1.05
0.26	0.20	0.12	0.4	0.30	0.24	0.25	0.25	0.20	0.35	0.15
7.59	3.70	5.14	12.6	6.51	8.52	9.34	8.52	3.30	6.37	3.54
58.8	47.8	38.7	47.2	30.4	39.2	42.1	14.0	10.7	10.5	10.6
23.9	18.1	12.4	35.6	24.4	23.4	25.0	18.1	12.6	24.5	9.20
38.8	22.8	17.0	60.6	24.6	29.5	51.2	31.3	39.1	54.6	38.8
239	204	193	240	134	170	188	87	57	33	56
7.08	6.00	5.46	7.40	4.30	5.17	5.70	3.01	2.00	1.07	1.88
3.20	1.80	2.14	8.60	3.03	3.52	9.78	4.75	5.80	7.26	5.79
25	23	22	32	23	23	24	24	25	27	25
77902	78220	76738	80125	79543	77955	78484	76103	75785	74364	75066
1.32	1.29	1.18	1.31	1.27	1.26	1.34	1.30	1.34	1.37	1.34
0.73	0.74	0.70	0.70	0.76	0.76	0.70	0.74	0.73	0.68	0.74
1.22	1.22	1.29	1.27	1.22	1.25	1.22	1.18	1.14	1.09	1.13
814	822	811	833	784	802	837	751	720	683	719
Cañada del Puerto area										
Bt-rich granite	Bt-Ap bodies							LFB[a]		KR[b]
NPE-5**	NPE-9**	NPE-10**	NPE-17**	NPE-19**	CON-2A	CON-2B	LNE-9	Av. $n=43$		Av. $n=5$
31°26′15.8″	31°25′46.4″	31°25′46.5″	31°25′46.0″	31°25′59.3″	31° 40’ 59.3”	31° 40’ 59.3”	31° 26’ 12.1”			
64°49′42.9″	64°49′49.8″	64°49′49.0″	64°49′49.8″	64°49′49.3″	64° 48’ 09.3”	64° 48’ 09.3”	64° 53’ 13.6”			
67.81	41.23	32.83	36.97	50.26	50.30	47.79	34.84	73.83		73.72
0.65	2.76	2.77	2.82	2.35	3.28	3.25	3.413	0.28		0.16
14.66	14.35	14.29	14.05	12.03	11.78	11.56	16.23	12.79		13.45
								0.84		
4.48	16.31	17.02	16.94	14.31	13.62	15.11	18.26	1.54		1.76
0.11	0.37	0.41	0.41	0.47	0.25	0.25	0.449	0.05		0.04
1.20	4.91	5.03	5.03	4.02	4.22	4.69	5.33	0.29		0.16
1.25	3.18	6.67	5.17	2.74	3.47	3.27	4.05	1.04		1.01
3.21	0.29	0.20	0.15	0.17	0.56	0.15	0.59	3.42		3.27
3.95	6.89	7.05	7.15	5.86	5.29	5.74	7.55	4.67		5.00
0.51	2.64	5.39	4.18	2.27	2.55	2.52	3.12	0.07		0.05
1.00	1.29	1.04	1.08	1.03	1.12	1.16	1.04	nd		0.92
98.83	94.22	92.71	93.93	95.52	96.46	95.49	94.89	98.82		99.53
21.70	95.3	103	139	61.2	27.3	28.6	78.3			
472	1486	1500	1709	1362	814	868	1400			
54	10	13	15	8	33	17	16			

Table 7 (continued)

108.7	143	148	163	107	209	248	189		
88.9	563	830	668	418	305	365	325		
205	1281	1900	1534	953	631	764	742	130	100
25.2	159	237	195	117	71.7	86.1	88		
94.5	586	888	706	437	257	306	331		
19.9	125	195	156	94.4	52.6	60.6	74.8		
1.1	5.34	8.80	7.04	4.41	4.67	5.18	3.29		
14.1	92.3	149	118	67.4	39.7	43.9	60.5		
2.1	14.4	23.6	18.8	10.5	6.37	6.87	10.2		
10.9	76.1	127	103	56.7	35.5	37.7	57.5		
1.80	12.9	21.8	18.0	9.70	6.40	6.77	10.2		
4.40	31.7	53.9	45.2	24.0	16.4	17.2	26.0		
0.60	4.41	7.60	6.48	3.33	2.27	2.44	3.63		
3.40	25.5	44.7	38.3	19.4	13.0	14.1	21.1		
0.50	3.5	6.3	5.28	2.63	1.74	1.91	2.89		
17.7	121	187	147	88.5	939	1866	95.3	5	10
74.4	479	674	540	335	189	246	113	24	51
49.1	365	617	310	377	180	182	280	71	65
64.8	291	276	509	257	1395	719	265	26	26
315	1674	2581	1986	1198	1081	1259	1362	322	185
9.3	51.5	79.6	62.5	36.6	26.7	34.7	39.0		
7.4	24.5	21.3	23.1	55.3	213	112	29.3		
31	55	54	55	52	49	48	67	22	24
77586	75944	75627	74356	63666	62342	61179	85894	67688	71181
1.38									
0.65									
1.22	2.24	4.06	3.22	1.87	2.15	2.18	2.86		
864									

Major element oxides and trace elements were analysed by ACTLABS Canada (*) and GeoAnalytical Lab, WSU, USA (**) (analytical details are found in Analytical methods Section). Total iron as Fe_2O_3 (ACTLABS) or FeO (GeoAnalytical Lab); major element oxides in wt.%, trace elements in ppm

T_{Zr} = 12,900/[2.95+0.85M+ln(496,000/Zr_{melt})], where $D^{Zr,zircon/melt}$ = (496,000/Zr_{melt}), is the ratio of Zr concentrations (ppm) in zircon to that in the saturated melt; M is a compositional factor that accounts for dependence of zircon solubility on SiO_2 and peraluminosity of the melt [(Na+K+2• Ca)/Al • Si), all in cation fraction. Geothermometer was calibrated for M=0.9 to 1.7. Equation and Zr concentrations (ppm) in zircon (= 496,000 ppm) from Miller et al. (2003)

Granitic rocks are monzogranites according to the Q-A-P modal of Streckeisen (1976).

ASI Aluminum Saturation Index = Al_2O_3/[(CaO-P_2O_5)+Na_2O+K_2O] (mol); *AI* Agpaitic Index = Na_2O+K2O/Al_2O_3 (mol). ASI and AI are reported for the granitic rocks

[a] The LFB average was taken from Chappell and White (1992). [b] The KR average was calculated using the data shown in Table 1 from Konopelko et al. (2007), using samples of the Uch-Koshkon felsic granite

1, 2, and 4 are granitic facies in Achala batholith, Bt-Ap bodies = Biotite-apatite bodies, NPE-5 is biotite-rich granite (see description in text). *nd* not determined

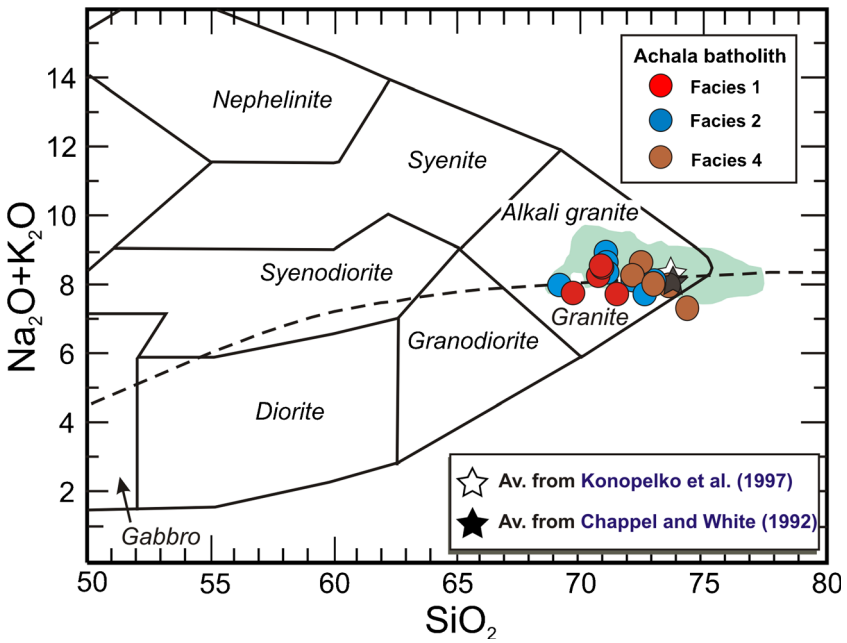

Fig. 5 SiO_2 vs. Na_2O+K_2O % variation diagram for the Achala batholith samples. The dyke and pale green field represents 46 Carboniferous granitic samples associated with the TIPA shear zone in the Sierras Pampeanas (Dahlquist et al. 2010). The star symbols are averages of A-type granitoids elsewhere from Konopelko et al. (2007) and Chappell and White (1992)

luminescent zoned cores are interpreted as a totally inherited older component.

The majority of the zircon ages are again concentrated at about 364 Ma and the age range of older inherited zircon is showed in Table 8. Five data points yield a Tera-Wasserburg Concordia age (Ludwig 2003) of 370±8 Ma (95 % confidence limits, again allowing for the uncertainty in U/Pb calibration). This is considered the best estimate for the crystallization of the host monzogranite (Fig. 9).

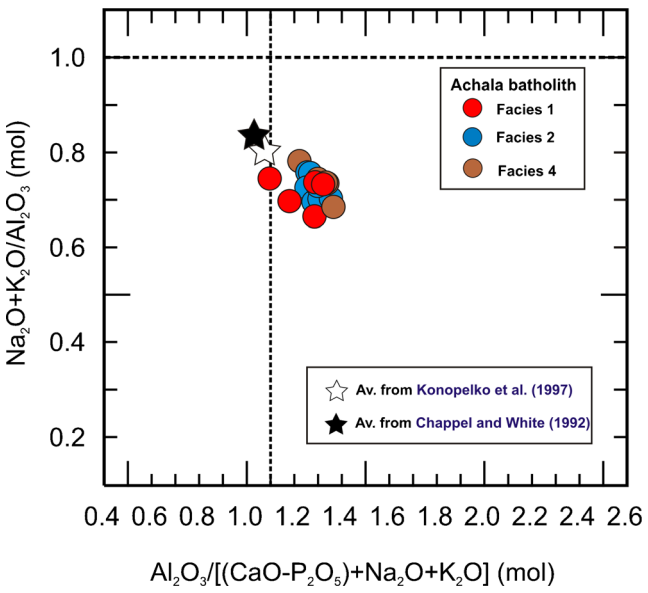

Fig. 6 Alumina saturation index (ASI) in the studied granitic rocks. Most of the samples are restricted to ASI=1.10–1.38, with relatively high values for the agpaitic index (> 0.65). ASI=1 from Shand (1927), ASI=1.1 from Chappell and White (1992)

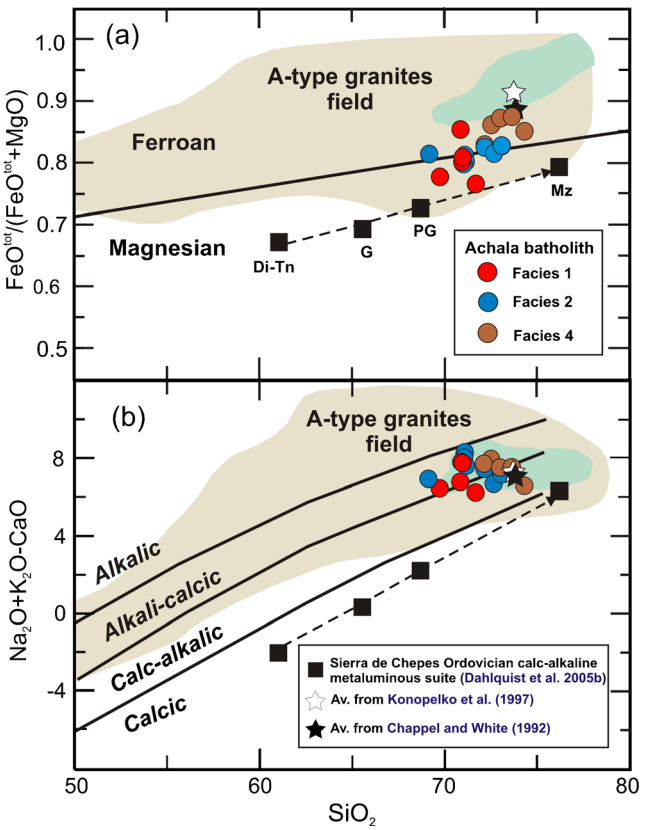

Fig. 7 Studied granites plotted in the classification diagrams of Frost et al. (2001): (**a**) Na_2O+K_2O-CaO vs. SiO_2, wt.% and (**b**) $FeO^t/(FeO^t+MgO)$ vs. SiO_2, wt.%. The A-type granite field is after Frost et al. (2001). A granitic Famatinian calc-alkaline suite is also plotted in this diagram (see text for discussion). Discontinuous line = Sierra de Chepes suite. Abbreviations: Di–Tn = diorites and tonalites, G = granodiorites, PG = porphyritic granodiorites, Mz = monzogranites (data from Dahlquist et al. 2005b)

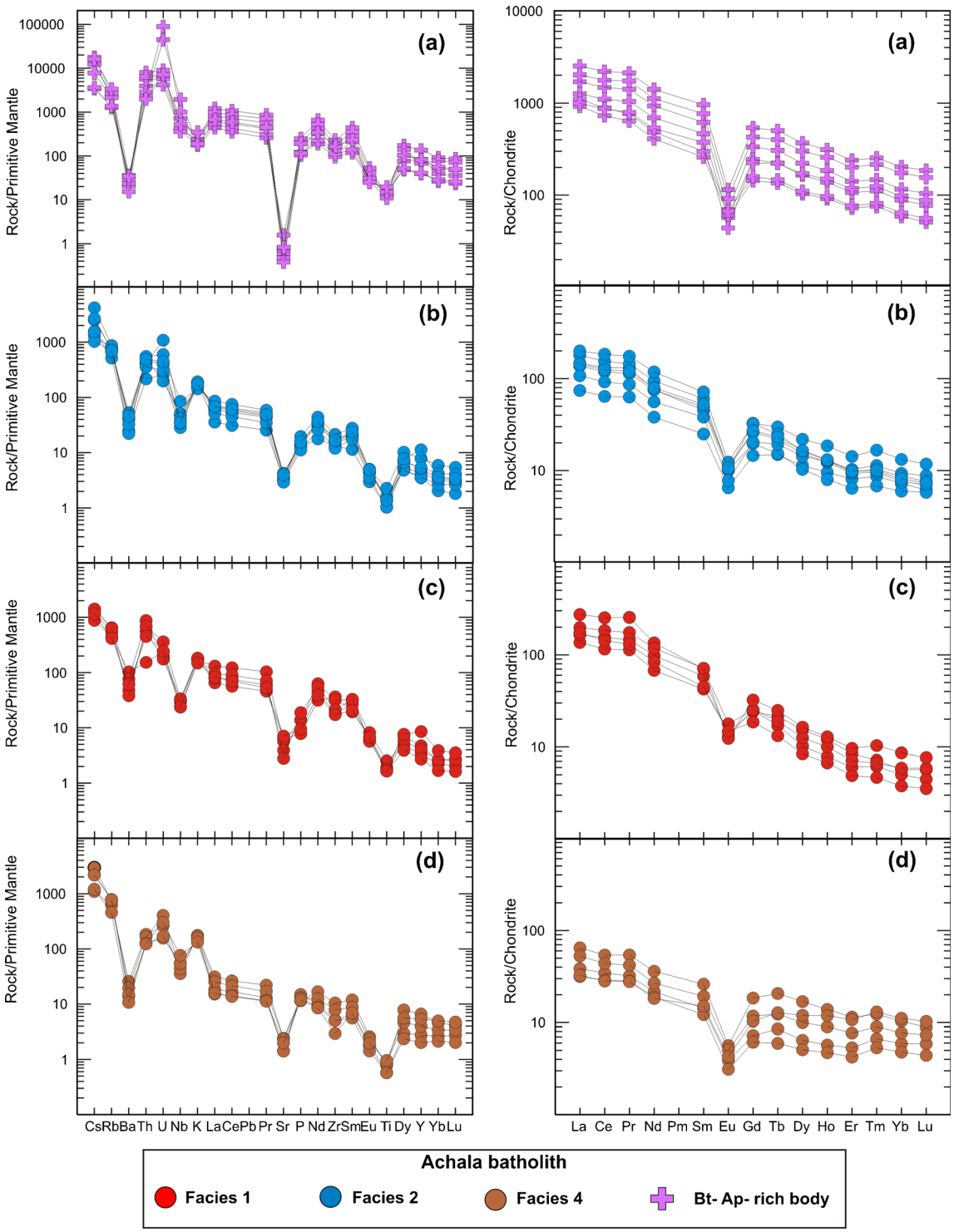

Fig. 8 **a**. Primitive-mantle normalized (Sun and McDonough 1989) spider diagrams. The granitic rocks have similar compositions to those reported for Carboniferous A-type granites of the Sierras Pampeanas (Dahlquist et al. 2010). **b** Chondrite-normalized (Nakamura 1974; Boynton 1984) REE plots. The rocks of the Achala batholith have REE patterns similar to those reported for Carboniferous A-type granites (Dahlquist et al. 2010), although the granitic rocks are impoverished in HREE. **b** Chondrite-normalized REE plots for biotite-apatite bodies, porphyritic granite, and monzogranite. Discussion of this Figure is carried out in Section Petrogenesis of the granitoid magmas

A large isotopic database including in situ U–Pb and Hf isotope data from magmatic zircon and whole-rock Sm-Nd isotopes was recently reported by Dahlquist et al. (2013) for the granitoids of Achala batholith. Epsilon Nd values (ε_{Ndt}) and Hf values (ε_{Hft}) were recalculated for the crystallization age of 369 Ma (average from ages of Achala batholith

Table 8 LA-ICP-MS zircon results for the monzogranite ACH-155 (facies 1) of the Achala Batholith

Grain spot	$^{238}U/^{206}Pb$	1σ	$^{207}Pb/^{206}Pb$	1σ	$^{206}Pb/^{238}U$ age	1σ	$^{207}Pb/^{206}Pb$ age	1σ	$^{207}Pb/^{235}Pb$ age	1σ
ACH-155 (P)										
ACH_155_2a	16.978	0.936	0.0594	0.0016	369	20	583	58	400	24
ACH_155_3a*	18.188	1.007	0.0538	0.0015	345	19	364	60	348	22
ACH_155_6a	4.979	0.276	0.0782	0.0021	1180	60	1153	53	1171	51
ACH_155_7a	16.584	0.912	0.0646	0.0017	377	20	760	56	437	26
ACH_155_8a	20.223	1.127	0.0569	0.0015	311	17	487	58	333	21
ACH_155_9a	11.156	0.629	0.0654	0.0018	553	30	788	56	602	34
ACH_155_12a*	16.350	0.897	0.0536	0.0011	383	20	354	44	379	20
ACH_155_13a	17.172	0.953	0.0622	0.0013	365	20	680	45	411	22
ACH_155_14a*	16.807	0.922	0.0541	0.0011	373	20	376	44	373	20
ACH_155_16a*	16.743	0.915	0.0537	0.0010	374	20	357	43	372	20
ACH_155_17a*	16.550	0.902	0.0540	0.0011	378	20	372	44	377	20
ACH_155_19a	18.815	1.054	0.0773	0.0015	334	18	1129	39	456	24

$^{238}U/^{206}Pb$ ratio corrected for static fractionation using Peixe (P)

Measurement errors represent within-run uncertainty only

$^{207}Pb/^{206}Pb$ ratios corrected for static fractionation using Peixe (P)

Asterisk (*) indicates data points used for Concordia age calculation

reported by Dahlquist et al. 2013). ε_{Hft} and ε_{Ndt} values are negative and vary between −3.6 to −5.8 (average=−4.4) and −4.0 to −6.5 (average=−4.8), respectively. Average T_{DM} Hf and T_{DM} Nd values range from 1.5–1.6 Ga and 1.4–1.6 Ga, respectively. More negative ε_{Hft} values (ranging from −10.7 to −17.6) were observed in one sample only (ACH-140, Supplementary Table 2 from Dahlquist et al. 2013).

Sample NPE-10, a typical biotite-apatite body, has a ε_{Ndt}= −5.7 and average ε_{Hft}=−3.6 (data from Dahlquist et al. 2013), which fall within the ranges for the analysed granitic rocks. Three further samples were analysed for their Nd isotopic composition (Table 9), yielding similar ε_{Ndt} and T_{DM} Nd values of -4.4 to -5.6 and 1.5 to 1.6 Ga, respectively. These isotopic data indicate an old continental lithosphere source.

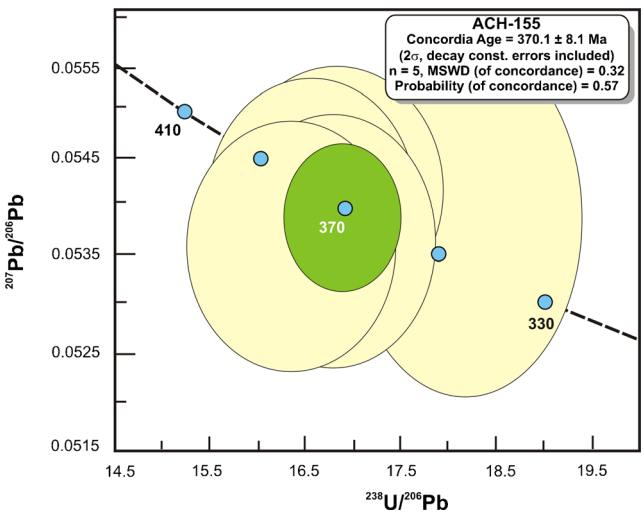

Fig. 9 U–Pb LA-ICP-MS zircon dating of monzogranite ACH-155 (facies 2) from the Achala batholith. The main Tera-Wasserburg plot shows most analyses plotting between 354 and 376 Ma and the inset shows a Concordia age of 370±8 Ma. The older ages are thought to represent retained inheritance and are reported in Table 8 only

Petrogenesis of the Achala batholith and biotite-apatite bodies

The whole-rock geochemical signatures and the biotite chemistry indicate that these Late Devonian granitic rocks are aluminous, F-rich, A-type granites. According to Eby (1990, 1992), A-type granites can be formed in a variety of ways: (i) fractionation of mantle-derived magma, (ii) reaction of mantle-derived magma with crustal rocks, (iii) partial melting of continental crust (metasomatized or not) (Abdel Rahman 2006; Konopelko et al. 2007). A petrogenetic model including (ii) has been invoked to explain the origin of Carboniferous A-type felsic melts in Sierras Pampeanas (see Dahlquist et al. 2010, 2013, Alasino et al. 2012 and references therein).

Biotite chemistry as indicator of their parental magmas

The studies of Abdel Rahman (1994) and Dahlquist et al. (2010 and references therein) demonstrate that the compositions of igneous biotites reflect the nature of their parental host magmas. In particular, Dahlquist et al. (2010) show that biotites crystallized from Early- to Mid-Ordovician calc-alkaline granitic magmas of the Famatinian orogen are

Table 9 Whole-rock Nd isotopes for biotite-apatite from Cañada del Puerto area, Achala batholith

Sample	[1]CA(t)	Sm *(ppm)*	Nd *(ppm)*	$^{147}Sm/^{144}Nd$	$(^{143}Nd/^{144}Nd)_{today}$	$(^{143}Nd/^{144}Nd)t$	$(^{143}Nd/^{144}Nd)t$ CHUR	εNd(t)	T_{DM} (Ga)	[2]T_{DM} (Ga)
CON-2B	369	60.6	306	0.1980	0.1196	0.511937	0.512163	−4.4	1.3	1.5
CON-2A	369	52.6	257	0.2050	0.1236	0.511925	0.512163	−4.6	1.4	1.5
NPE-17	369	156	706	0.2210	0.1336	0.511876	0.512163	−5.6	1.6	1.6
Average	369							−4.9	1.4	1.5

The decay constants used in the calculations are the values $\lambda\ ^{147}Sm=6.54\times10^{-12}$ $year^{-1}$ recommended by the IUGS Subcommision for Geochronology (Steiger and Jäger 1977). Epsilon-Nd (εNd)t values were calculated relative to a chondrite present day: ($^{143}Nd/^{144}Nd$)today CHUR=0.512638; ($^{143}Sm/^{144}Nd$)today CHUR=0.1967. t = time used for the calculation of the isotopic initial ratios

[1] *CA* Crystallization age

[2] T_{DM} calculated according to De Paolo et al. (1991). Epsilon Nd values (ε_{Ndt}) calculated for the crystallization age t = 369 Ma (average from ages of Achala batholiths reported by Dahlquist et al. 2013)

significantly different from those biotites from the A-type Early Carboniferous granitic magmas of the Sierras Pampeanas. Biotites crystallized in Ordovician calc-alkaline, Early Carboniferous A-type, and Middle-Late Devonian Achalian granites have distinctive FeO/MgO ratios and F content. Thus, FeO/MgO ratios together with F contents of igneous biotites seem to reflect the nature of their parental host magmas and may be useful in identifying kinship (e.g., Dahlquist et al. 2010).

Biotites from the calc-alkaline suite of the Famatinian orogen are moderately enriched in MgO with $FeO^t/MgO=1.72–1.76$ and occupy a narrow field in the MgO vs. FeO^t diagram (Fig. 10a). Biotites from Ordovician peraluminous rocks, such as the Tuaní granite, plot below the general trend of the Ordovician metaluminous calc-alkaline biotites (Fig. 10a) and have $FeO^t/MgO=1.64$. Biotites in the Carboniferous A-type plutons have very high FeO relative to MgO, with $FeO^t/MgO=8.46–59.52$ and mostly plot in the field of anorogenic alkaline granites (Fig. 10a). In contrast, studied biotites from the Achala batholith have high FeO^t/MgO (3.03 – 3.95) and plot in the peraluminous granite field (Fig. 10a).

Distinctive $Fe^{2+}/(Fe^{2+}+Mg)$ ratios and F content are observed for the Ordovician, Devonian and Carboniferous granitoids rocks of Sierras Pampeanas (Table 3, Fig. 10b). Achala biotites have remarkably high F contents (F=0.89–2.32 %) compared with those in Ordovician granitoids (F=0 to 0.37, Dahlquist et al. 2010) but similar to those in the A-type Carboniferous granites. However, F content of biotites in facies 2 and the biotite-apatite-rich bodies are extremely high (1.21 to 2.32 %). In general, the biotites composition in Achala batholith strongly suggests high F content in the magma.

Petrogenesis of the granitoid magmas

Zircon saturation thermometry of Watson and Harrison (1983) provides a simple and robust means of estimating magma temperatures for both metaluminous and peraluminos rocks (Miller et al. 2003). Given that these are peraluminous granites, the zircon geothermometer of Watson and Harrison (1983) can be used to estimate magmatic temperatures. Miller et al. (2003) conclude that this geothermometer can be used for either inheritance-rich or inheritance-poor granitoids. The calculated results for M values between 0.9 and 1.7 (the calibration range for the geothermometer) are: facies 1, equigranular monzogranites with scarce Kfs phenocrystals=843±29 °C; facies 2, porphyritic monzogranites=809±17 °C; and facies 4, equigranular monzogranites=729±26 °C (Table 7). These temperatures values are consistent with those obtained from granitic rocks.

A crude correlation between the calculated temperature and the Eu anomaly and SiO_2 is observed for each granitic facies. Consistently, the temperature decreases as the Eu anomaly becomes more negative and the SiO_2 content increases (Table 7), giving confidence to the values obtained using the zircon geothermometer. NPE-7 sample (facies 4) represents a late granitic dyke emplaced in facies 1 and 2, and yields the lowest temperature, 683 °C.

Chondrite-normalized REE plots and primitive mantle-normalized spider diagrams (Fig. 8) show several distinctive features. (1) REE patterns tend to be flat to slightly LREE enriched and have significant negative Eu anomalies indicating that feldspar fractionation or residual feldspar in the source region played a role in the petrogenesis of the magmas (Fig. 8). (2) Significant negative Ba and Sr anomalies in the spider diagrams similarly support the important role of feldspar (Fig. 8). (3) Significant negative Ti and positive P anomalies indicate that Ti oxides, apatite, and monazite also played a role. (4) LIL elements are significantly enriched with respect to primitive mantle.

Logarithmic plots of Eu versus Ba and Sr concentrations show linear trends for the granitic rocks of the central area of the Achala batholith (Fig. 11). Both Ba and Sr decrease with decreasing Eu (Fig. 11), showing the role of feldspar fractionation in the evolution of these magmas. In the case of perfect fractional crystallization for a particular pluton or complex, the samples will form a linear trend that shows the relative proportions of K-feldspar and plagioclase fractionating from

the magma. If this proportion changes as the magma evolves the trend will be curved. Linear trends for a number of the suites indicate that K-feldspar and plagioclase fractionated in an approximately equal proportions (Fig. 11). Therefore, both fractional crystallization (including feldspar) and residual feldspar in the source region are both invoked for the generation of these A-type granites. However, some scattering of the data beyond analytical error suggests that the system was not entirely closed and that there was some interaction with the surrounding rocks during the emplacement of the magma.

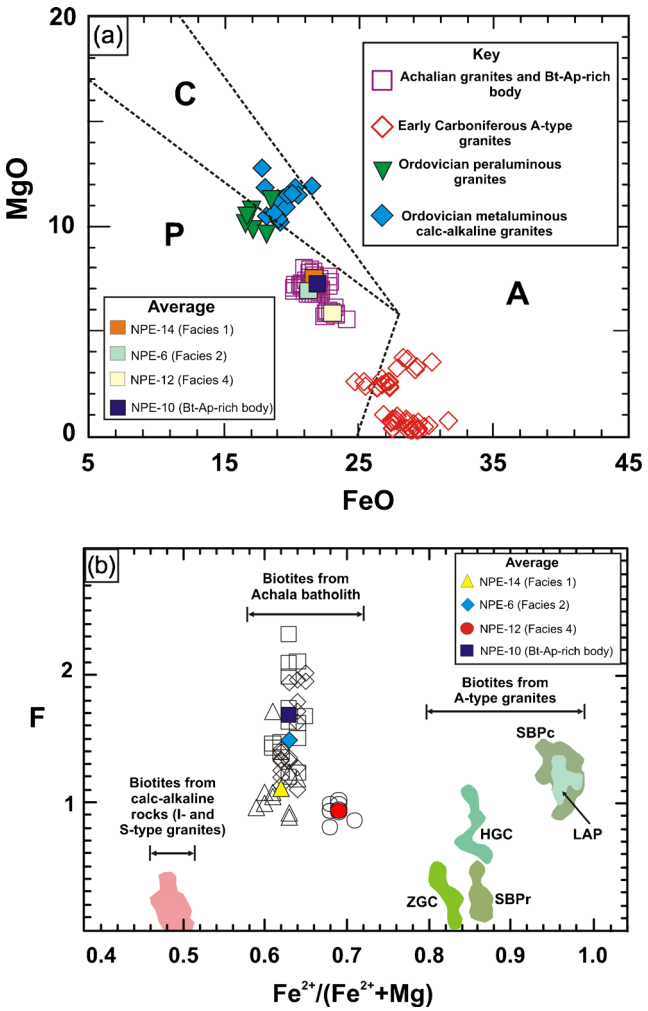

Fig. 10 **a**. Mineral chemistry for biotites in calc-alkaline metaluminous and peraluminous granites of Early Ordovician age and in the studied granites (biotites from facies 1, 2, 4, and biotite-apatite body). FeO vs. MgO biotite discriminant diagram after Abdel Rahman (1994): biotite in anorogenic alkaline suites (A field), biotite in peraluminous granites (P field), and biotite in metaluminous calc-alkaline granite suites (C field). **b**. The F content in biotite range from 0 to 0.37 %, 0.25 to 1.43 %, and 0.81 to 2.32 % for Ordovician metaluminous calc-alkaline and peraluminous granites, Early Carboniferous A-type granites, and Achala granites, respectively (the data from biotites crystallized in Ordovician and Carboniferous granites are of Dahlquist et al. 2010). Abbreviations: ZGC = Zapata Granitic Complex, SBPr = San Blas pluton rim zone, SBPc = San Blas Pluton core zone, HGC = Huaco Granitic Complex, LAP = Los Árboles Pluton

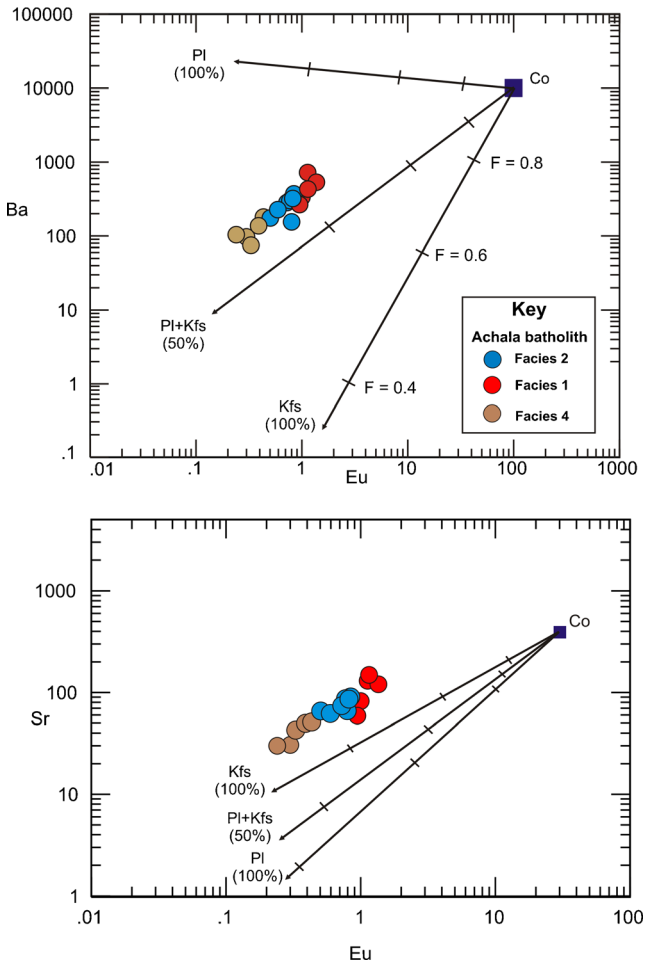

Fig. 11 **a** Ba vs. Eu and **b** Sr vs. Eu. Linear trends for a number of the suites indicate that K-feldspar (Kfs) and plagioclase (Pl) crystallize in an approximately 50:50 ratio. The partition coefficient data for minerals in equilibrium with granitic liquids are from Icenhower and London (1996), Ewart and Griffin 1994, Nash and Crecraft (1985), and Philpotts and Schnetzler (1970). The crystallization percentage for Kfs and Pl is indicated in the figure. Co = Initial concentration, F = weight fraction of remaining melt

Significant positive P anomalies referred above is distinctive of peraluminous A-type Achala granites. Early Carboniferous A-type granites in the Sierras Pampeanas have negative P anomalies (Dahlquist et al. 2010). These A-type granites represent variable mixtures of asthenospheric mantle and continental crust (Dahlquist et al. 2010), while isotopic data indicate that Achala granites were derived from a continental source (Dahlquist et al. 2013 and this work). The positive P anomaly in Achala granites (and previous geochemical data such as high ASI, etc.) is consistent with a continental source, mainly metasedimentary since P (together with volatile elements such as F) is a common element in sedimentary rocks (Taylor and McLennan 1985; Nelson 1992).

The high Ga/Al ratio is a distinctive or typical characteristic of the A-type granites, and plots of these ratios against major and trace element data readily distinguish these granites from

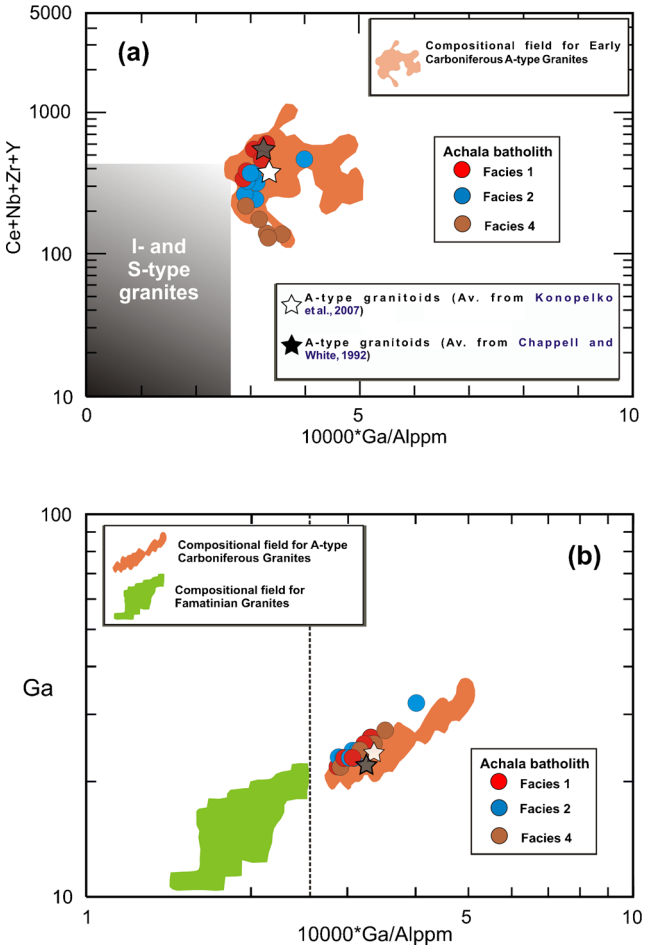

Fig. 12 **a** Ce+Nb+Zr+Y vs. 10,000×Ga/Al granite discrimination diagram (Whalen et al. 1987). **b** Al_2O_3, CaO, and Ga diagrams showing the compositions of the studied granites of the Achala batholith, the Early Carboniferous A-type granites (orange field) and the Famatinian calc-alkaline granitoids (green field). For the Famatinian calc-alkaline granitoids the SiO_2 content ranges from tonalites (SiO_2=60 wt.%) to monzogranites (SiO_2=75 wt.%). Chemical data for the Famatinian granitoids are from Dahlquist et al. (2005b, 2008) and for the Early Carboniferous A-type granites from Dahlquist et al. (2010). The 10,000*Ga/Al discrimination limit for A-type granites is from Whalen et al. (1987). Ai and Aii are A-type average compositions from Konopelko et al. (2007) and Chappell and White (1992), respectively

I-type (calc-alkaline) and S-type granites (Whalen et al. 1987). Thus, using the Ga vs. Ga/Al diagram, A-type granites of the Achala batholith are distinguished from the calc-alkaline granites from the Famatinian orogen (Ordovician) and strongly support the A-type designation for these granites (Fig. 12a, b). According to Whalen et al. (1987), Ga is enriched relative to Al because the latter is preferentially trapped in residual plagioclase, while Ga is stabilized in the melt in GaF_6^{-3} structures during melting of an F-enriched source.

Our database of chemical analysis of biotite from calc-alkaline magmas (I- and S-type) and A-type granites in the proto-Andean margin indicates that biotite composition depends largely upon the nature of the magma, as was originally suggested by Abdel Rahman (1994).

As was referred in Section "Biotite chemistry as indicator of their parental magmas", the biotites in the Achala granites (Table 3 and Fig. 10b) have distinctively high F content (0.89–2.32 %), strongly suggesting that the magmas had relatively high HF/H_2O ratios. This high F content together with relatively high $[Fe^{2+}/(Fe^{2+}+Mg)]$ ratios in biotite (0.62 to 0.69) is a typical feature of A-type granites (Dahlquist et al. 2010 and references therein). Thus, FeO/MgO ratios together with F content of igneous biotites seem to reflect the nature of their A-type parental host magmas. However, the relatively high Al^{IV} (2.39 to 2.58 a.p.f.u) and the occurrence of primary muscovite indicate that the micas crystallized from aluminous magma, as noticed by Lira and Kirschbaum (1990) and Rapela et al. (2008a).

Based on discrimination diagrams using Y and Rb vs. SiO_2 (Pearce et al. 1984) and invoking the dominant peraluminous composition of granitic rocks studied from the Achala batholith Lira and Kirschbaum (1990) conclude that these granites have S-type affinities and are consistent with within-plate tectonic setting. However, Y vs. Nb, Ta vs. Yb or Y vs. SiO_2 plot (Figure not included) of Pearce et al. (1984), intended as a granite discrimination plot, the Achala samples scatter between the fields for volcanic-arc/syncollisional granites and within-plate granites. There is large overlap in Y and Yb concentrations between the granitic rocks, and the diagrams do not help to determine the tectonic setting. As noticed in previous papers, these diagrams do not work satisfactorily. Twist and Harmer (1987) studied granites and felsites using a large database and noted that the trace-element signatures of these rocks do not identify their tectonic setting per se.

Source of the granitoid magmas of Achala batholith

Based on large isotopic database for the granitoids of Achala batholith, Dahlquist et al. (2013) concluded that the generation of Devonian magmas dominantly involved crustal reworking and stabilization rather than the formation of new continental crust by juvenile material accretion.

Petrogenetic models for A-type granites commonly invoke igneous source rocks (e.g., Collins et al. 1982; Creaser et al. 1991; Frost and Frost 1997) and peraluminous A-type granites are uncommon. Fayalite granite is a member of the most reduced A-type granites, commonly thought to have been primarily sourced from tholeiitic rocks. Huang et al. (2011) have reported fayalite-bearing A-type granite produced by high temperature melting of granulitic metasedimentary rocks. Dahlquist et al. (2010) concluded that A-type granites represent variable mixtures of asthenospheric mantle and continental crust and that different mixtures lead to different (and numerous) subtypes (illustrating the lack of consensus about A-type magma origin, Bonin 2007). King et al. (1997) suggested that A-type granites in the Lachlan Fold Belt of SW Australia were derived from the partial melting of an infracrustal felsic source, leading to the formation of

'aluminous' (metaluminous and weakly peraluminous) A-type granites. Alternatively, the Achala batholith could represent a subtype of A-type granite derived from a crustal source with a dominant metasedimentary component, as indicated by our whole-rock and mineral chemistry and the Nd isotope data (see Section Geochronological data and isotope geochemistry of the Achala batholith, Biotite chemistry as indicator of their parental magmas, and Petrogenesis of the granitoid magmas).

Petrogenesis of the biotite-apatite bodies: A discussion

Although the data presented here are not fully conclusive with regard to the origin of the unusual biotite-apatite bodies, new studies are being conducted to elucidate their petrogenesis because they represent concentrations of uranium and REE with economic potential.

Dorais et al. (1997) concluded that the identical age of the biotite-apatite bodies (which they termed enclaves) and the host granites (368±2 Ma), coupled with textural, mineralogical, and bulk-rock characteristics of the apatite bodies, indicated that they are magmatic segregations, i.e., cumulates formed by fractional crystallization in a closed system, without significant contamination of the magma during its evolution. This is supported by the indistinguishable ε_{Ndt} values of the granitic rocks and biotite-apatite-rich bodies (data from Dahlquist et al. 2013 and this work). However, this model has some relevant unresolved problems if we consider the classical definition of cumulates (Wager 1963): 'homogeneous nucleation and growth produces primary precipitates (or *primocrysts*) that reach coarse sizes before being deposited as "cumulus" crystals'. The cumulate model supports subsequent sinking of the cumulate to the bottom of the magma chamber. This model is assumed by Dorais et al. (1997) to explain the origin of the biotite-apatite bodies, as shown in the Fig. 13 of the referred paper. However, sheet silicate, zircon and monazite have very different densities (zircon=4.7, monazite=5.1, biotite=3.1, and muscovite=2.8 gr/cm3) and accumulation and subsequent sinking of all these minerals together is unrealistic.

Alternatively, we suggest that accessory minerals crystallized early and that biotite and muscovite then nucleated on these seeds (or alternatively grew synchronously). Subsequently, the micas were then accumulated, probably by flow segregation. Thus, we have accumulation of biotite and muscovite plus the accessory minerals in the mica crystals. In this model the density of the minerals is not a factor as it is not gravity settling.

Evidence of differential laminar flow is clearly shown in some dyke-like biotite-apatite bodies, where K-feldspar phenocrysts are transferred from the host granite (Fig. 3l) and concentrated in the centre of dyke while increasing in size (e.g., Komar 1972; Ross 1986; Philpotts and Ague 2009).

Other observed structures such as repetitive layering (Fig. 3k) strongly suggest an origin by compacting piles of crystal mush, where different minerals previously crystallized are expelled leading to the development of "inch-scale" layering (Boudreau 1995). Field and petrographic observation shows that K-feldspar phenocrysts and quartz were transferred from the granite (see Section Field occurrence and petrography description). The referred structures are compatible with flow segregation of crystals (e.g., Paterson 2009).

Paterson (2009) concluded that diverse magmatic structures such as pipes, tubes pipes, troughs, diapirs, and plume heads are formed by local magma flow through crystal-mush host magmas, being often related with the formation of schlieren-rich in accessory and mafic minerals, and are associated with filter pressing and accumulation of crystals with diverse magma histories and ages.

Our main conclusion is that the enrichments of these trace elements (including U) did not occur during the differentiation of the melt but was effected during earlier flow segregation. Thus, the high concentrations of accessory minerals (plus biotite and muscovite) lead to the formation of Bt-Ap bodies with economic interest. These bodies are not cumulates sensu stricto i.e., solid rocks early formed and sinking from a parental magma. The high trace elements concentration in Bt-Ap bodies (representing earlier-crystallized) strongly suggest a parental magma derived of a continental source that is supported by the isotopic data (see Dahlquist et al. 2013 and this work) while the high Al_2O_3, P, U, and F contents strongly suggest the presence of a metasedimentary source.

Conclusions

The main conclusions of this study are:

1) The precise U-Pb LA-ICP-MS zircon age from ACH-155 confirm that the Achala batholith was emplaced in Late Devonian time.
2) The geological setting for the Achala batholith is complex. Our whole-rock data reveal that the granitic rocks are Al-rich throughout the narrow range of silica content (69.8 to 74.5 %), and show dominant geochemical signatures typical of A-type granites but strongly enriched in Al. Thus, the whole-rocks composition strongly suggests crystallization from '*peralumious A-type magma*'.
3) Our petrogenetic model supports progressive fractional crystallization, dominant of feldspar, explaining the distinctive negative Eu anomalies typically observed in A-type granites.
4) Igneous muscovite and distinctive biotite compositions with high FeO/MgO ratios, Al^{IV} and F, indicate crystallization from '*F-rich peraluminous A-type parental magma*'.
5) The similar isotope compositions for granites and biotite-apatite bodies here studied indicate a common continental source.
6) Biotite and muscovite nucleated on seeds or earlier-crystallized accessory minerals (or alternatively grew

synchronously with them). Subsequently, the micas were then physically accumulated, probably by flow segregation. Thus, Bt-Ap bodies preserve an earlier record of the petrogenesis of the Achala batholiths. The high Al_2O_3, P, U, and F contents indicate metasediments in the source.

Acknowledgments Financial support was provided by PICT 1009 (FONCyT), PID 2008 MINCyT Cba 000121, PIP CONICET 1940, and a CONICET external fellowship awarded to J.A. Dahlquist for his research stay at Washington State University, supervised for the Professor J. Vervoort. J.A. We thank C. Casquet (UCM) and E. Baldo (CONICET-UNC) for the early discussion about this work. Dahlquist thanks R.J. Pankhurst for his English review and F. Colombo for the analysis using JEOL JXA-8230 electron microprobe. Thorough reviews by two anonymous reviewers and the assistant of the associated editorG.Hoinkes and the editor in Chief R. Abart resulted in a major improvement of the original manuscript. We are very grateful to them.

References

Abdel Rahman AM (1994) Nature of biotites from alkaline, calc-alkaline, and peraluminous magmas. J Petrol 35:525–541

Abdel Rahman AM (2006) Petrogenesis of anorogenic peralkaline granitic complexes from eastern Egypt. Mineral Mag 70:27–50

Alasino PH, Dahlquist JA, Pankhurst RJ, Galindo C, Casquet C, Rapela CW, Larrovere M, Fanning CM (2012) Early Carboniferous sub- to mid-alkaline magmatism in the Eastern Sierras Pampeanas. NW Argentina: a record of crustal growth by the incorporation of mantle-derived material in an extensional setting. Gondwana Res 22:992–1008

Armstrong JT (1988) Quantitative analysis of silicates and oxide minerals: Comparison of Monte-Carlo, ZAF and Phi-Rho-Z procedures. In: Newbury DE (ed) Microbeam analysis. San Francisco Press, California, pp 239–246Baldo EGA (1992) Estudio petrológico y geoquímico de las rocas ígneas y metamórficas entre Pampa de Olaen y Characato. Extremo norte de la Sierra Grande de Córdoba. República Argentina. Tesis Doctoral (Ph.D.), Universidad Nacional de Córdoba, (*unpublished*). pp. 305

Bonin (2007) A-type granites and related rocks: evolution of a concept, problems, and prospects. Lithos 97:1–29

Boudreau AE (1995) Crystal aging and the formation of fine-scale igneous layering. Mineral Petrol 54:55–69

Boynton WV (1984) Geochemistry of the rare earth elements: Meteorites studies. In: Henderson P (Ed.), Rare earth element geochemistry. Elsevier. 63–114 pp

Casquet C, Pankhurst RJ, Rapela CW, Dahlquist J, Baldo EG, Galindo C, Fanning CM (2011) Short-lived plutonism coeval with sediment underplating and high-grade metamorphism in the inner Famatinian magmatic arc of the Sierras Pampeanas, Argentina. VII Hutton Symposium on Granites and Related Rocks: p. 33. Avila, Spain, 4–9 July

Chang Z, Vervoort JD, McClelland WC, Knaack C (2006) U-Pb dating of zircon by LA-ICP-MS. Geochem Geophys Geosyst 7:1–14

Chappell BW, White AJR (1992) I- and S- type granites in the Lachlan Fold Belt. Trans R Soc Edinb Earth Sci 83:1–26

Clarke DB, Dorais M, Barbarin B, Barker D, Cesare B, Clarke G, el Baghdadi M, Erdmann S, Förster H-J, Gaeta M, Gottesmann B, Jamieson RA, Kontak DJ, Koller F, Gomes CL, London D, Morgan VIGB, Neves LJPF, Pattison DRM, Pereira AJSC, Pichavant M, Rapela C, Renno AD, Richards S, Roberts M, Rottura A, Saavedra J, Sial AN, Toselli AJ, Ugidos JM, Uher P, Villaseca C, Visona D, Whitney DL, Williamson B, Woodard HH (2005) Occurrence and origin of andalusite in peraluminous felsic igneous rocks. J Petrol 46:441–472

Collins WJ (2002) Hot orogens, tectonic switching, and creation of continental crust. Geology 30:535–538

Collins WJ, Beams SD, White AJR, Chappell BW (1982) Nature and origin of A-type granites with particular reference to southeastern Australia Contrib Mineral Petrol 80:189–200

Creaser RA, Price RC, Wormald RJ (1991) A-type granites revisited: assessment of a residual-source model. Geology 19:163–166

Dahlquist JA, Rapela CW, Baldo E (2005a) Petrogenesis of cordierite-bearing S-type granitoids in Sierra de Chepes, Famatinian orogen, Argentina. J S Am Earth Sci 20:231–251

Dahlquist JA, Rapela CW, Pankhurst RJ, Baldo E, Saavedra J, Alasino PH (2005b) Los granitoides de la sierra de Chepes y su comparación con granitoides paleozoicos de las Sierras Pampeanas: implicancias para el orógeno famatiniano. Geología de la provincia de La Rioja — Precámbrico–Paleozoico Inferior: In: Dahlquist, J.A., Baldo, E.G., Alasino, P.H. (Eds.), Asociación Geológica Argentina, Serie D, Publicación Especial, 8: pp. 87–108 (In Spanish)

Dahlquist JA, Pankhurst RJ, Rapela CW, Casquet C, Fanning CM, Alasino P, Baez FM (2006) The San Blas Pluton: an example of Carboniferous plutonism in the Sierras Pampeanas, Argentina. J S Am Earth Sci 20:341–350

Dahlquist JA, Galindo C, Pankhurst RJ, Rapela CW, Alasino PH, Saavedra J, Fanning CM (2007) Magmatic evolution of the Penón Rosado granite: petrogenesis of garnet-bearing granitoids. Lithos 95:177–207

Dahlquist JA, Pankhurst RJ, Rapela CW, Galindo C, Alasino P, Fanning CM, Saavedra J, Baldo E (2008) New SHRIMP U–Pb data from the Famatina complex: constraining Early–Mid Ordovician Famatinian magmatism in the Sierras Pampeanas, Argentina. Geol Acta 6:319–333

Dahlquist JA, Alasino PH, Eby GN, Galindo C, Casquet C (2010) Fault controlled Carboniferous A-type magmatism in the proto-Andean foreland (Sierras Pampeanas, Argentina): geochemical constraints and petrogenesis. Lithos 115:65–81

Dahlquist JA, Rapela CW, Pankhurst RJ, Fanning CM, Vervoort JD, Hart G, Baldo EG, Murra JA, Alasino PH, Colombo F (2012) Age and magmatic evolution of the Famatinian granitic rocks of sierra de Ancasti, Sierras Pampeanas, NW Argentina. J S Am Earth Sci 34:10–25

Dahlquist JA, Pankhurst RJ, Gaschnig RM, Rapela CW, Casquet C, Alasino PH, Galindo C, Baldo EG (2013) Hf and Nd isotopes in Early Ordovician to Early Carboniferous granites as monitors of crustal growth in the Proto-Andean margin of Gondwana. Gondwana Res 23:1617–1630

De Paolo DJ, Linn AM, Schubert G (1991) The continental crustal age distribution: methods of determining mantle separation ages from Sm–Nd isotopic data and application to the Southwestern United States. J Geophys Res 96:2071–2088

Dickinson WR, Gehrels GE (2003) U-Pb ages of detrital zircons from Permian and Jurassic eolian sandstones of the Colorado Plateau, USA: paleogeographic implications. Sediment Geol 163:29–66

Dorais MJ, Lira R, Chen Y, Tingey D (1997) Origin of biotite–apatite-rich enclaves, Achala batholith, Argentina. Contrib Mineral Petrol 130:31–46

Ducea MN, Otamendi JE, Bergantz G, Stair KM, Valencia VA, Gehrels GE (2010) Timing constraints on building an intermediate plutonic arc crustal section: U- Pb zircon geochronology of the Sierra Valle Fértil–La Huerta, Famatinian arc, Argentina. Tectonics 29: doi: 10.1029/2009TC002615

Eby GN (1990) The A-type granitoids: a review of their occurrence and chemical characteristics and speculations on their petrogenesis. Lithos 26:115–134

Eby GN (1992) Chemical subdivision of the A-type granitoids: petrogenetic and tectonic implications. Geology 20:641–644

Ewart A, Griffin WL (1994) Application of proton-microprobe data to trace-element partitioning in volcanic-rocks. Chem Geol 117:251–284

Franchini M, Lira R, Meinert L, Ríos FJ, Poklepovic MF, Impiccini A, Millone H (2005) Na-Fe-Ca Alteration and LREE (Th-Nb) Mineralization in marble and granitoids of Sierra de Sumampa, Santiago del Estero, Argentina. Econ Geol 100:733–764

Frost CD, Frost BR (1997) Reduced rapakivi-type granites: the tholeiite connection. Geology 25:647–650

Frost BR, Barnes CG, Collins WJ, Arculus RJ, Ellis DJ, Frost CD (2001) A geochemical classification for granitic rocks. J Petrol 42:2033–2048

Galindo C, Pankhurst RJ, Casquet C, Coniglio JE, Baldo E, Rapela C, Saavedra J (1997) Age, Sr and Nd isotope systematics, and origin of two fluorite lodes, Sierras Pampeanas, Argentina. Int Geol Rev 39: 948–954

Galliski MA (1994) La Provincia Pegmatítica Pampeana. II: Metalogénesis de sus distritos económicos. Rev Asoc Geol Argent 49:113–122

Gaschnig RM, Vervoort JD, Lewis RS, McClelland WC (2010) Migrating magmatism in the northern US Cordillera: in-situ U-Pb geochronology of the Idaho batholith. Contrib Mineral Petrol 159: 863–883

Grosse P, Söllner F, Baéz MA, Toselli AJ, Rossi JN, de la Rosa JD (2009) Lower Carboniferous post-orogenic granites in central-eastern Sierra de Velasco, Sierras Pampeanas, Argentina: U–Pb monazite geochronology and Sr–Nd isotopes. Int J Earth Sci 98:1001–1025

Höckenreiner M, Söllner F, Miller H (2003) Dating the TIPA shear zone: an early Devonian terrane boundary between the Famatinian and Pampean systems (NW Argentina). J S Am Earth Sci 16:45–66

Huang HQ, Li XH, Li WX, Li ZX (2011) Formation of high $\delta^{18}O$ fayalite-bearing A-type granite by high-temperature melting of granulitic metasedimentary rocks, southern China. Geology 39:903–906

Icenhower JP, London D (1996) Experimental partitioning of Rb, Cs, Sr, and Ba between alkali feldspar and peraluminous melt. Am Mineral 81:719–734

Jarosewich EJ, Nelen JA, Norberg JA (1980) Reference samples for electron microprobe analysis. Geostand Newslett 4:43–47

Johnson DM, Hooper PR, Conrey RM (1999) XRF analysis of rocks and minerals for major and trace elements on a single low dilution Li-tetraborate fused bead. Adv X-ray Anal 41:843–867

King PL, White AJR, Chappel BW, Allen CM (1997) Characterization and origin of aluminous A-type granites from the Lanchan Fold Belt, Southern Australia. J Petrol 38:371–391

Komar PD (1972) Flow differentiation in igneous dikes and sills: profiles of velocity and phenocryst concentration. Geol Soc Am Bull 83: 3443–3448

Konopelko D, Biske G, Seltmann R, Eklund O, Belyatsky B (2007) Hercynian postcollisional A-type granites of the Kokshaal Range, Southern Tien Shan, Kyrgyzstan. Lithos 97:140–160

Kretz R (1983) Symbols for rock-forming minerals. Am Mineral 68:277–279

Lira R (1985) Un nuevo modelo metalogenético uranífero en el basamento cristalino de las Sierras Pampeanas: uranio en metamorfitas de contacto (Batolito de Achala – Pcia. De Córdoba). Bol Asoc Geol Córdoba 7:438–451

Lira R, Kirschbaum AM (1990) Geochemical evolution of granites from the Achala batholith of the Sierras Pampeanas, Argentina, in: Kay SM, Rapela CW (Eds.), Plutonism from Antarctica to Alaska. Geological Society of America Special Paper 241: pp. 67–76

López de Luchi MG, Siegesmund S, Wemmer K, Steenken A, Naumann R (2007) Geochemical constraints on the petrogenesis of the Palaeozoic granitoids of the Sierra de San Luis, Sierras Pampeanas, Argentina. J S Am Earth Sci 24(2–4):138–166

Ludwig KR (2003) Isoplot 3.0. A Geochronological Toolkit for Microsoft Excel. Special Publication, 4. Berkeley Geochronological Center, Berkeley, CA 94709, USA

Martino R (2003) Las fajas de deformación dúctil de las Sierras Pampeanas de Córdoba: Una reseña general. Rev Asoc Geol Argent 58:549–571

Martino R, Kraemer P, Escayola M, Giambastiani M, Arnosio M (1995) Transecta de las Sierras Pampeanas de Córdoba a los 32° S. Rev Asoc Geol Argent 50(1–4):60–77

McGuire AV, Francis CA, Dyar MD (1992) Mineral standards for electron microprobe analysis of oxygen. Am Mineral 77:1087–1091

Miller CF, Stoddard EF, Bradfish LJ, Dollase WA (1981) Composition of plutonic muscovite. Genetic implications. Can Mineral 19:25–34

Miller CF, McDowell SM, Mapes RW (2003) Hot and cold granites? Implications of zircon saturation temperatures and preservation of inheritance. Geology 31:529–532

Nakamura N (1974) Determination of REE, Ba, Mg, Na and K in carbonaceous and ordinary chondrites. Geochim Cosmochim Acta 38:757–773

Nash WP, Crecraft HR (1985) Partition coefficients for trace elements in silicic magmas. Geochim Cosmochim Acta 49:2309–2322

Nelson DR (1992) Isotopic characteristic of potassic rocks. Evidence for the involvement of subducted sediment in magma genesis. Lithos 28:403–420

Pankhurst RJ, Rapela CW (1998) The proto-Andean margin of Gondwana: An introduction, in: Pankhurst RJ, Rapela CW (Eds.), The Proto-Andean Margin of Gondwana. Geological Society of London, Special Publications 142:1–9

Pankhurst RJ, Rapela CW, Saavedra J, Baldo EG, Dahlquist JA, Pascua I, Fanning, CM (1998) The Famatinian arc in the central Sierras Pampeanas: an Early to Mid-Ordovician continental arc on the Gondwana margin. In: Pankhurst RJ, Rapela CW (Eds.), The Proto-Andean Margin of Gondwana: Geological Society of London, Special Publication, 142:343–367

Pankhurst RJ, Rapela CW, Fanning CM (2000) Age and origin of coeval TTG, I–S-type granites in the Famatinian belt of NW Argentina. Trans R Soc Edinb Earth Sci 91:151–168

Paterson SR (2009) Magmatic tubes, troughs, pipes, and diapers: late-stage convective instabilities resulting in compositional diversity and permeable networks in crystal-rich magmas of the Tuolumne Batholith, Sierra Nevada, California. Geosphere 5:496–527

Patiño Douce MLG, Patiño Douce AE (1987) Petrología y petrogénesis del batolito de Achala, provincia de Córdoba, a la luz de la evidencia de campo. Rev Asoc Geol Argent 42:201–205

Pearce JA, Harris NBW, Tindle AG (1984) Trace element discrimination diagrams for the tectonic interpretation of granitic rocks. J Petrol 25: 956–983

Philpotts JA, Schnetzler CC (1970) Phenocryst-matrix partition coefficients for K, Rb, Sr and Ba, with applications to anorthosite and basalt genesis. Geochim Cosmochim Acta 34:307–322

Philpotts A, Ague J (2009) Principles of igneous and metamorphic petrology. Cambridge University Press. pp. 684

Pinotti L, Coniglio J, Esparza A, D'Eramo F, Llambías E (2002) Nearly circular plutons emplaced by stoping at shallow crustal levels, Cerro Áspero batholith, Sierras Pampeanas de Córdoba, Argentina. J S Am Earth Sci 15:251–265

Pinotti L, Tubía JM, D'Eramo F, Vegas N, Sato AM, Coniglio J, Aranguren A (2006) Structural interplay between plutons during the construction of a batholith (Cerro Aspero batholith, Sierras de Córdoba, Argentina). J Struct Geol 28:834–849

Rapela CW (1982) Aspectos geoquímicos y petrológicos del batolito de Achala, provincia de Córdoba. Rev Asoc Geol Argent 37:313–332

Rapela CW, Pankhurst RJ, Bonalumi AA (1991) Edad y geoquímica del pórfido granítico de Oncán, Sierra Norte de Córdoba, Sierras

Pampeanas, Argentina. 6 Congreso Geológico Chileno, Resúmenes Expandidos: 19–22

Rapela CW, Pankhurst RJ, Casquet C, Baldo E, Saavedra J, Galindo C, Fanning M (1998) The Pampean orogeny of the southern proto-Andes: Cambrian continental collision in the Sierras de Córdoba, in: Pankhurst RJ, Rapela, CW (Eds.), The Proto-Andean Margin of Gondwana. Geological Society of London, Special Publications 142: 181–217

Rapela CW, Pankhurst RJ, Casquet C, Fanning CM, Baldo EG, González-Casado JM, Galindo C, Dahlquist J (2007) The Río de la Plata craton and the assembly of SW Gondwana. Earth Sci Rev 83:49–82

Rapela CW, Baldo EG, Pankhurst RJ, Fanning CM (2008a) The Devonian Achala batholith in the Sierras Pampeanas: F-rich aluminous A-type granites. VI South American Symposium on Isotope Geology, San Carlos de Bariloche, Argentina, Proceedings in CD-ROM, Paper 53

Rapela CW, Pankhurst RJ, Dahlquist JA, Baldo EG, Casquet C, Galindo C (2008b) Revisiting accretionary history and magma sources in the Southern Andes: Time variation of "typical Andean granites". 7 International Symposium on Andean Geodynamics, Nice, France, Extended Abstracts: 427–430

Rasband WS (2011) ImageJ, U. S. National Institutes of Health, Bethesda, Maryland, USA, http://imagej.nih.gov/ij/, 1997–2011

Ross ME (1986) Flow differentiation, phenocryst alignment, and compositional trends within a dolerite dike at Rockport, Massachusetts. Geol Soc Am Bull 97:232–240

Saavedra J, Baldo EG, Pankhurst, RJ, Rapela CW, Murra J (1998) El granito de Capilla del Monte (Sierras Pampeanas de Córdoba, Argentina): edad, geoquímica, génesis y especialización metalogenética. 10 Congreso Latinoamericano de Geología y 6 Congreso Nacional de Geología Económica 2: 372

Scheepers R (2000) Granites of the Saldania mobile belt, South Africa: radioelements and P as discriminators applied to metallogeny. J Geochem Explor 68:69–86

Schwartz JJ, Gromet LP, Miró R (2008) Timing and duration of the calc-alkaline arc of the Pampean Orogeny: implications for the Late Neoproterozoic to Cambrian evolution of western Gondwana. J Geol 116:39–61

Shand SJ (1927) The eruptive rocks. John Wiley, New York, 360 pp

Siegesmund S, Steenken A, López de Luchi MG, Wemmer K, Hoffmann A, Mosch S (2004) The Las Chacras–Potrerillos batholith (Pampean Ranges, Argentina): structural evidence, emplacement and timing of the intrusion. Int J Earth Sci 93:23–43

Simpson C, Law R, Gromet L, Miró R, Northrup C (2003) Paleozoic deformation in the Sierras de Córdoba and Sierra de Las Minas, eastern Sierras Pampeanas, Argentina. J S Am Earth Sci 15:749–764

Sims JP, Ireland TR, Camacho A, Lyons P, Pieters PE, Skirrow RG, Stuart-Smith PG, Miró R (1998) U-Pb, Th-Pb and Ar-Ar geochronology from the southern Sierras Pampeanas, Argentina: implications for the Palaeozoic tectonics evolution of the western Gondwana margin, in: Pankhurst RJ, Rapela CW (Eds.), The Proto-Andean Margin of Gondwana. Geological Society of London, Special Publications 142: 259–281

Speer JA (1984) Micas in igneous rocks, in: Bailey SW (Ed.), Micas, Reviews in Mineralogy 13: 299–356

Steiger RH, Jäger E (1977) Subcommission of geochronology: convention on the use of decay constants in geo- and cosmochronology. Earth Planet Sci Lett 36:359–362

Streckeisen A (1976) To each plutonic rock its proper name. Earth Sci Rev 12:1–33

Stuart-Smith PG, Miró R, Sims JP, Pieters PE, Lyons P, Camacho A, Skirrow RG, Black LP (1999) Uranium-lead dating of felsic magmatic cycles in the southern Sierras Pampeanas, Argentina: implications for the tectonic development of the proto-Andean Gondwana margin, in: Ramos VA, Keppie JD (Eds.), Laurentia Gondwana connections before Pangea. Geological Society of America Special Publication 336: 87–114

Sun SS, McDonough, WF (1989) Chemical and isotopic systematics of oceanic basalts; implications for mantle composition and processes. Magmatism in the ocean basins: In: Saunders AD, Norry MJ (Eds.), Geological Society of London 42: 313–345

Taylor SR and McLennan SM (1985) The continental crust: its composition and evolution. Blackwell Scientific Publications. Great Britain. pp 312

Twist D, Harmer REJ (1987) Geochemistry of contrasting siliceous magmatic suites in the Bushveld complex: genetic aspects and implications for tectonic discrimination diagrams. J Volcanol Geotherm Res 32:83–98

Wager LR (1963) The mechanism of adcumulus growth in the alyered series of the Skaergaard intrusion: Mineralogical Society of America Special Paper 1: 1–9

Watson EB, Harrison TM (1983) Zircon saturation revisited: temperature and composition effects in a variety of crustal magma types. Earth Planet Sci Lett 64:295–304

Whalen JB, Currie KL, Chappell BW (1987) A-type granites: geochemical characteristics, discrimination and petrogenesis. Contrib Mineral Petrol 95:407–419

Willner AP, Gerdes A, Massonne HJ, Schmidt A, Sudo M, Thomson SN, Vujovich G (2011) The geodynamics of collision of a microplate (Chilenia) in Devonian times deduced by the pressure–temperature–time evolution within part of a collisional belt (Guarguaraz complex, W-Argentina). Contrib Mineral Petrol 162:303–327

Wilson M (1989) Igneous petrogenesis: A global tectonic approach. Chapman & Hall, London, 466 pp

Zarco JJ (2006) Geología estructural y petrología del complejo granítico peraluminoso de Achala en relación con la génesis y localización de mineralizaciones de uranio (Sierras Pampeanas - Argentina). Tesis Doctoral (Ph.D.), Universidad Nacional de Salta, Argentina (*unpublished).* pp. 147